Fall 2021

Mechanical Strength of Sic Composite Tubing Under Uniaxial and Multiaxial Loading

Colton Corley

MECHANICAL STRENGTH OF SiC COMPOSITE TUBING UNDER UNIAXIAL AND MULTIAXIAL LOADING

by

Colton Corley

Bachelors of Science
University of South Carolina, 2019

Submitted in Partial Fulfillment of the Requirements

For the Degree of Master of Science in

Mechanical Engineering

College of Engineering and Computing

University of South Carolina

2021

Accepted by:

Xinyu Huang, Director of Thesis

JingJing Bao, Reader

Tracey L. Weldon, Interim Vice Provost and Dean of the Graduate School

DEDICATION

This thesis is dedicated to my support system of family and friends who supported me through the ups and downs of working through grad school. Without them I would not have been able to complete my Master's degree, and I am forever thankful.

ACKNOWLEDGEMENTS

In these acknowledgements I would like to thank the M.E. Department of the University of South Carolina, my research advisor Dr. Xinyu Huang, Dr. Jack Bao, and collaborator George Jacobson of General Atomics for their assistance in guiding this project and providing the tools to accomplish it. With a year impacted by the Coronavirus, the patience and understanding that was provided to me in order to complete my degree is something that will not be lost on me, and is something I greatly appreciate. The things I learned working under Dr. Huang and Dr. Bao are also something that I will be forever grateful, as they were instrumental in helping me grow and develop my knowledge. The previous work in our research group to hone some of the methods in this study are also greatly appreciated, as their work was also instrumental in building up this study.

ABSTRACT

Silicon carbide fiber reinforced silicon carbide matrix composite is one of the candidate materials for accident tolerant nuclear fuel cladding concepts. In a Nuclear power plant, the reactions between the fuel, cladding, and coolant in a potential loss of coolant accident(LOCA) are of utmost importance to ensure safety in the accident tolerance of such plants. It is for this reason that SiC(silicon carbide) composite tubes have been selected as a possible alternative to the older Zirconium based cladding methods currently used in the industry, which were a partial cause of the Fukushima 2011 meltdown. To serve as fuel cladding, a material must be able to withstand certain stresses and strains in high temperature environments, and the use of SiC composite is due to its low reactivity with steam and it's capability or maintaining high strength at high temperature. In studying the SiC composite to ensure its safety in actual usage, many different techniques are being employed to create a full knowledge of the material. The goal of this study is to better understand the mechanical behavior of SiC composite tubing, particularly its mechanical strength under uniaxial and multi-axial loading situations.

This will be accomplished by compiling testing results for multiple uniaxial and multiaxial testing scenarios. These include, burst testing, axial testing, torsion testing, torsion-burst testing, and tension-torsion testing. By encapsulating all 5 of these testing scenarios, the general profile of a sample's failure strength can be created as a function of principal stress direction in the sample.

The analysis of the various strengths of the material in different conditions were accomplished by various measurement methods. These methods were comprised of stress and strain observation and calculations, through use of strain gauges and general stress measurement techniques and equations, DIC digital image correlation to verify loading angles and strains created by testing, AE acoustic emission to analyze sample failure by use of sound analysis and matrix/fiber failure events, and x-ray computed tomography(XCT) to analyze post-failure samples.

Samples were tested accordingly to map a failure profile for samples with the specific triaxial fiber architecture. This failure map was created to show the ability of a sample to resist failure when the principal stress is pointed to a given direction on the samples. The triaxially braided samples provided by General Atomics showed an abnormal weakness in torsional loading, which has a 45° principal stress angle. The samples proved strongest in the 2 uniaxial testing methods, and the samples in combined loading had the notable strength drop-off the closer the principal stress load angle reached 45° from either starting at 0° (hoop) or 90° (tensile). The samples had the highest tensile strength in the axial direction, due to the triaxial braid giving the most support to tensile loading due to fiber orientation. It was hypothesized after post processing that torsional strength drop-off could be due to the braid angle and orientation.

TABLE OF CONTENTS

LIST OF FIGURES

LIST OF ABBREVIATIONS

AE ..... Acoustic Emission

CFCC ..... Ceramic Fiber Ceramic Composite

CMC ..... Ceramic Matrix Composite

CVI ..... Chemical Vapor Infiltration

DIC ..... Digital Image Correlation

ID ..... Inside Diameter

OD ..... Outside Diameter

PLS ..... Proportional Limit Stress/Strength

SiC ..... Silicon Carbide

SiC_f/SiC_m ..... Silicon Carbide Fiber Reinforced Matrix Composite

XCT ..... X-ray computed tomography

UTS ..... Ultimate Tensile Stress/Strength

CHAPTER 1. INTRODUCTION

1.1 Background

The purpose of the individual research project being conducted is to better understand and characterize the mechanical behaviors of SiC_f/SiC_m composite nuclear cladding. This specifically will be done through a multitude of different tests being conducted on the tubular samples, with different combined loading tests completed to find and document the mechanical behaviors of the samples. The underlying backdrop of this project is the studies of SiC_f/SiC_m material as an alternative to zirconium based cladding following the Fukushima Daiichi nuclear disaster. This meltdown of Zirconium cladding tubes after the loss of coolant is a critical vulnerability of current light water reactors in the field, so research has been done to find new methods and expand the options available.

In order to fully characterize the SiC samples, much research needs to be done to fully define its behaviors under various stresses during normal operation and accident conditions. SiC_f/SiC_m composite is a material that exhibits pseudo-ductile and anisotropic behavior. Specifically, this project will focus on exploring its anisotropic strength by using various testing methods. These single loading tests can be combined except for tension and burst, allowing for a range of multiple tests that can be used to determine different mechanical outcomes. These different tests can then be used to create a broad reaction envelope of the target samples by comparing the results of different loading conditions to see a difference in behavior over different conditions. By doing this, the knowledge of the behavior of these samples can be better defined and better represented. The goal of better

representing this will be done by testing different samples from the same batch in the different tests, allowing for close comparison. Tests of hoop, tension, torsion, tension-torsion, burst-torsion will be done to find results for the stress-strain behavior of the samples by use of strain measuring techniques, most generally strain gauges and other complementary measurements accompanying it such as AE and DIC. These will be used to then carry out a calculation of mechanical properties of the samples to better understand their reactions in theory. Studies like this have been carried out before, as in the case of Shapovalov and Bernachy-Barbe et al, which involved the use of uniaxial and biaxial loading conditions as well in order to characterize SiC cladding samples in their tubular form as much as possible [1, 2]. These studies can be used as a basis of knowledge to understand the reasoning and process in how this study was carried out as well.

The Fukushima Daiichi nuclear disaster in 2011 prompted research of alternative nuclear fuel and cladding materials with high accident tolerance [3]. In a paper carried out to address the gap between R&D efforts and actual usage in real time scenarios, it was noted that a large reason for the consideration of SiC_f/SiC_m composite cladding was due to its capabilities in preventing runaway melting of control rods and unwanted reactions in a meltdown scenario, giving an extra blanket of safety and more time before unwanted reactions in theoretical severe accident situations [4]. Combined with new fuel pellets, the combination is very attractive to explore as an alternative to current field used strategies [4]. This thermal condition of ensuring that fuel clad do not melt before fuel pellets in a meltdown is key to ensuring a reaction like that of the Fukushima 2011 disaster do not repeat themselves again. Compared to the older Zirconium alloy claddings used in current generation reactors, SiC_f/SiC_m cladding is highlighted by a study by Hallstadius et al [5].

This study, done in 2012, summarized that the SiC cladding has numerous strengths over the old gen Zirconium alloy claddings. One of the leading reasons for this is the little to no corrosion and hydrogen creation during normal operating conditions as well as severe accident scenarios, a leading problem for the Zirconium-alloy cladding failure of 2011, and that it retained its strength at higher temperatures, a downfall of Zirconium-alloy cladding [5]. These mentioned findings all point towards the reasoning of developing and exploring a material such as SiC composite tubing as an alternative cladding.

1.2 SiC_f/SiC_m Material/Characterization

Before looking into the mechanical characteristics of the SiC_f/SiC_m composite, it is important to look into the material build and makeup. The monolithic SiC material by itself is a strong and brittle material, with high strength and high thermal conductivity. SiC_f/SiC_m composite consists of strong SiC fibers (grouped in strands) and SiC matrix which infiltrated into the fiber preform using chemical vapor infiltration (CVI) process [6]. A study by Deng et al [7] was centered around looking at different fuels with higher thermal conductivity. This study was centered around this due to the challenges of using SiC cladding in real use scenarios, because of the possibility of brittle failure of the material, which is important to get around as a problem [7]. This study pointed to the reasoning for having SiC but also the downfalls, i.e., the brittle nature of the material... This brittle failure of the SiC monolithic material can be circumvented by the addition of the SiC fibers. This allows the composite material to have a pseudo-ductile behavior, as the fibers can withstand stress even while the matrix itself is behaving in a brittle manner, giving itself a pseudo-ductile failure, as stated by Deck [8].

The main load carrying portion of a SiC_f/SiC_m composites is the SiC fiber. This portion generally consists of a weave of fibers going in different directions. For example, there might be 3 sets of fiber directions, with one running along the axial direction of a tubular sample, one running +45° from that axial direction, and one running -45° from that line. This is done to add strength to the material by having multiple directions in which the fiber tows can take on load from any situation. The final fiber preform generally resembles a type of basket weave, with fibers going under and over fibers that run in different angle and directions.. The fiber architecture can be tailored to the loading condition of the part. According to the study done by C.P. Deck et al [3], SiC fibers performed well against and were shown to have high strength compared to alternatives for reinforcement of the SiC samples. After forming the fiber preform, generally a layer of interface material between the fiber and matrix is deposited to allow for weak bonding between the fiber and the SiC matrix. This layer can have a great effect on the outcome of debonding and separation of the material, according to a study done by Fellah et al [9].

The process to create the SiC_f/SiC_m composites involves making the SiC fiber preform first, and then adding the matrix phase. This can be accomplished by using a process called Chemical Vapor Infiltration(CVI) [6]. This process involves the use of a chemical process that deposits the material onto a woven strand of the SiC fibers, allowing for a combination of woven matrix and composite that gives the combined effects of both the composite and the fibers [6]. The mechanical properties of how this effects the damages of the samples has been explored in other studies as well, and can be partially seen in the effects of this study, although it will not be gone into in depth.

The previously mentioned process can be used in different ways, giving way for different architecture of SiCf/SiCm samples. The samples in this study specifically are of a triaxial braid architecture, which has three fiber orientations running in the sample, combined with the deposited chemical composite portion forming the composite and matrix combination. In some scenarios previously, the methods of this study had also been used on different samples sets with different makeups, for the purpose of further analysis of those separately, and to develop the method more, so the process and setup is not specific to this orientation of samples. Previous studies into the mechanical behaviors of SiC_f/SiC_m composite have been done by this research group and General Atomics to this end. In one of these studies, the compilation of mechanical properties was also done by combining results into a failure envelope of mechanical behavior [1]. In this study, it was theorized that the behavior of the samples when in failure was generally graceful, showing that this type of material can still exhibit aspects of its shape relatively well even after breaking. This behavior is important due to ensuring that the SiC_f/SiC_m can maintain some form to keep fuel inside the cladding when it has even gone past the limit of its strength. If a sample were to break and exhibit large amounts of visible damage, this could lead to problems. In previous testing done with this test setup prior to the batch specified, the samples also generally held shape, and showed repeatable forms of damage. Repeatable damage mechanisms are a way to show the sample is behaving in the same way under a test parameter, so paying attention to these was key as well in testing samples. The layout of a generic triaxial weave can be seen in figure 1.1.

The material specifically provided by GA for this project is detailed as follows. General Atomics – Electromagnetics Systems Group (GA-EMS) identified, fabricated and

delivered sets of SiGA® Tubes (Silicon Carbide Composite) to USC. Braid architectures were collaboratively chosen with USC to provide failure envelopes for architectures that cover both hoop and axial biased braid types. Details of the architecture of these braids are included in table 1.1.

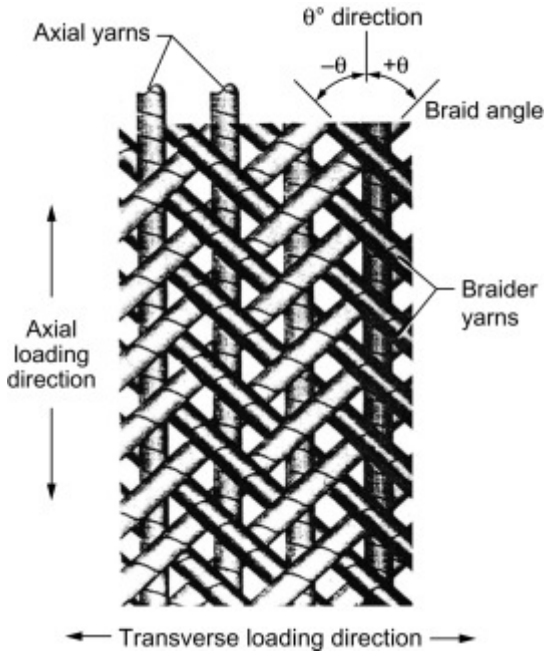

Figure 1.1, Triaxial braid diagram [10]

Table 1.1, Details of Fiber Preforms Used for Tube Fabrication

Fiber	Braid Architecture	Bias Angle	Plies	Weave	Axial Tows
Hi Nicalon Type S	Triaxial	45	2	1 over 1	12

Fabrication of these specimens took place using standard GA-EMS procedures used for the DOE-NE Accident Tolerant Fuel program. This includes a thin pyrolytic interphase coating deposited directly on the fibers and a crystalline SiC matrix deposited using

chemical vapor infiltration. While SiGA® cladding is expected to have a monolithic overcoat for gas tightness, fundamental properties of the SiC composite is easier to analyze without this overcoat present.

1.3 Measurement Techniques

In order to measure behavior of the samples, multiple techniques were used. These techniques included the use of strain gauges, , DIC strain measurement techniques, AE measurement, and XCT scanning. Starting off, the use of Omega linear and shear gauges was key to the strain measurement of samples.

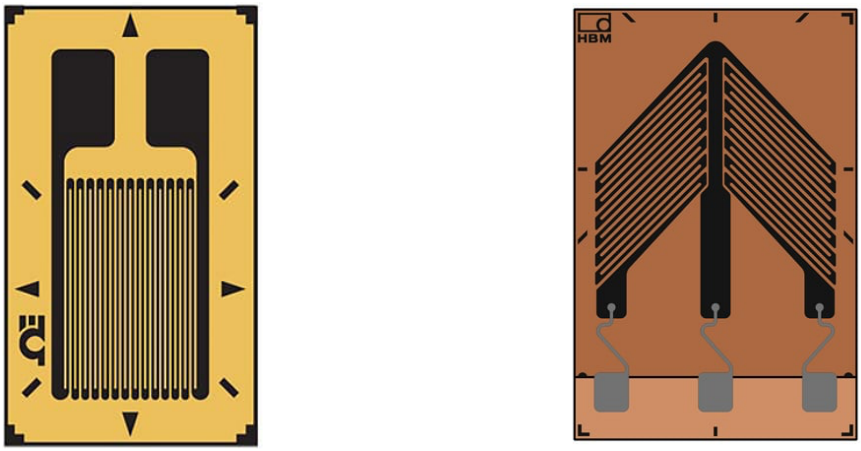

Figure 1.2, Typical linear and shear strain gauges

By attaching these strain gauges on the samples in various manners, such as in the hoop and axial directions for the linear strain gauges, and in the shear direction for the double 45 gauge, allowed for accurate reading of sample strain in a localized manner. A DAQ was used to gather the Strain gauge data as well as other load cell and pressure data used in

testing. Using variants of quarter bridge, half bridge, and full bridge setups, different strain measuring techniques could be accomplished while also canceling out any parasitic strain components unwanted in the measurements, such as residual bending strains on the sample.

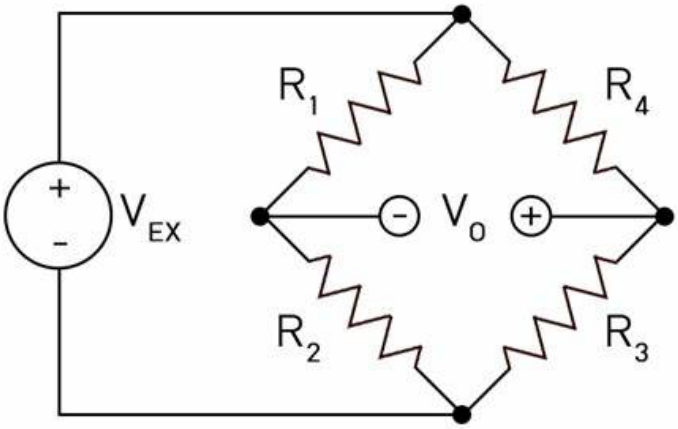

Figure 1.3, Wheatstone bridge

By using various combinations of external wiring and internal setup in a DAQ, the different loading conditions could be measured in the specific way needed for it. For instance, in any torsional loading, the use of a double 45 strain gauge was used. This strain gauge requires the use of a half bridge setup, which involves the use of two of the 4 resistor slots in the above graphic. By using a quarter bridge, which is how the hoop and tension strain gauges are wired, the calculation for the strain of those articles can be found as well. The equation for calculation strain can be generally found from Omega strain gauges' handbook [11]. Vr is the result of measuring the voltage change between input and output from the unstrained position and the strained position. Using this, the strain for a single strain gauge can be found.

$$Strain = \frac{-4 * Vr}{GF(1 + 2Vr)}$$

$$\mathrm{Vr} = \frac{\mathrm{VOUT}}{\mathrm{VIN}}[\text{strained}] - \frac{\mathrm{VOUT}}{\mathrm{VIN}}[\text{unstrained}]$$

Eq. 1.1, Strain calculation

The DAQ device that is used to process the strain does these calculations internally, and gives a strain value as a result. Using the gauges, any single direction of strain can be measured if desired as well as shear strain in any direction on the tubular sample, giving the combinations required to measure the strains of all 5 tests done effectively. The set up of the strain gauges on the samples to read all of the strain readings which are necessary for this study are done with a 0° orientation and 90° orientation for the axial and hoop strain setup, and a double 45° shear strain gauge in -45° and +45° directions to measure shear strain. This strain, combined with postprocessing of stress data, would then be used to create accurate stress-strain relation curves for the samples involved.

1.4 AE Measurement Technique

The next part of measurement techniques used for this paper include the AE measurement system. The system used for the tests ran in this study is the MISTRAS PCI-II AE monitoring system, in conjunction with the AEwin software, using wideband AE sensors purchased from Physical Acoustics. This wideband HD2WD sensor is a miniature version of the normally offered general use sensor by physical acoustics, allowing for it to fit onto smaller portions of the samples. This version can be seen detailed in figure 1.4, showing the end sensor of the model used in this study that would be attached onto the samples during testing.

Figure 1.4, Physical Acoustics AE sensor (model HD2Wd)

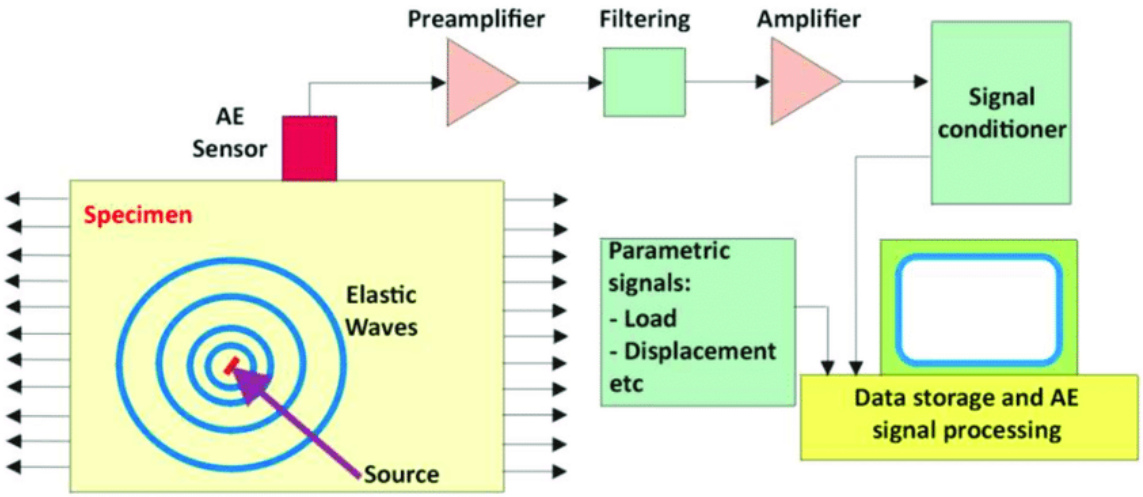

Figure 1.5, AE system explanation [12]

This AE sensor is applied using hot melt glue and padding to enable for a secure attachment to the sample, with a thin enough barrier to reduce AE signal attenuation. This AE sensor is connected by a thin cable to an amplifier, and then to the computer which received the signal. The computer then would record the signal in hit and time recorded variants, allowing for processing according to each individual AE event and across the entire timeframe of the test. This was useful due to being able to record every hit's energy, as this was key to later analysis in the study.

AE measurement can be helpful due to its use in assisting with the calculation of a sample's PLS, or proportional limit stress, in a test. During the process of damaging a CMC sample, specifically SiC_f/SiC_m, it is known previously that matrix microcracking and debonding from the interphase between the materials can be a sign of damage in the sample, and this damage can produce loud sounds that can be analyzed [9]. Previous studies have been done on this effect and how it can be used and analyzed in the case of mechanical testing, such as done by Morscher, and some new studies even propose ways to analyze specific damage mechanisms based on AE strength and signals with other combined methods, such as in Maillet et al [13, 14]. In these studies, use of AE to describe damage onset in samples is used to help better characterize the failure of the samples and the reasons for it. Using AE data, methods of identifying various strength limits of the material can be carried out by use of AE analysis and pre-set parameters and criteria. In studies by both Nozawa et al and Liu et al, methods for comparing AE onset stress and actual PLS levels were carried out for better analysis and pinpointing of PLS [15, 16]. In Liu, the use of 4 different methods to create a PLS which was verified was a focus in the study. In this paper, the methods followed from that paper were the PLS eyeball method and PLS offset strain method combined with the AE onset method, which was the method produced by using calculation from AE and stress data. In this same study by Liu, a method for characterizing so called 'loud' AE events was utilized [15]. This was the method for which AE PLS was defined in this study, using a method of characterizing AE events into loud events, and using a threshold of at least 10% of the loudest AE event not including final failure on a sample test by AE energy, or aJ, as the threshold for what constitutes a loud AE event. By using this metric, and combining it with criteria set in this study of the first cluster of loud

events or first handful of loud events recorded, the method for which the AE PLS was obtained using the AE analysis. The hit-stamp AE data was pulled from the computer and interpolated in stress-strain data for the samples, allowing for accurate lining up of sample data and AE energy data.

1.5 DIC Imaging Technique

The next portion of sample measurement included in this study was the use of DIC digital image correlation strategies. DIC is a method to observe strain displacements by use of a high definition camera, and use of a gradient image pattern that shifts as a result of displacement and can be recorded easily. Previous studies done on SiC samples and general stress strain response samples have already proven it to be a reliable method for contributing to strain measurement, and there are multiple iterations of it in research literature as a method of measuring strain changes, or even fiber architecture and damage initiation [17, 18, 19]. In these studies, DIC was a tool in measuring multiple different desired phenomena, such as the previously mentioned strain and damage mechanisms, showing its capabilities as a method of measurement in the realm of strain and damage initiation. DIC as a method of measuring strain during a test in the case of this study is used as a supplementary method, to measure and compare to physically measured strain with a gauge, but more importantly to verify the stress-strain loading parameters utilized in the tests. By utilizing DIC, the angle of principal stress can be verified by the ability to produce color maps highlighting points and spots of high strain concentration. This strain concentration will follow a direction that is driven by the loading conditions, showing where the sample is being displaced the most. In the case of the 5 tests used in this study, this meant that the combination loading and basic loading settings could be verified by

checking these color maps of principal strain, which show the combination of strain experienced by the sample. In an axial /tensile test, this strain colormap and reading will show high localized strain of the sample pulling apart axially, and in a hoop burst test, it will show the sample with high localized strain coming apart along the long spine of the sample. In the loading case of shear/torsion loading, the strain will display effects of the natural 45° principal strain in torsion. When torsion loading is combined with the tensile or internal pressure methods, the sample will show effects of both conditions, showing an angle of loading that is in between the angle of either 0°-45° or 45°-90° depending on the type of test. The general angle of strain as a result of the loading combinations can be used in conjunction with principal stress calculations to verify the loading angle for a test. Due to the nature of material failure for SiC cladding samples, it can be hard to perfectly pre-calculate certain failure parameters or ratios of the two combination loading scenarios, so rough estimates are made with a general range in mind.

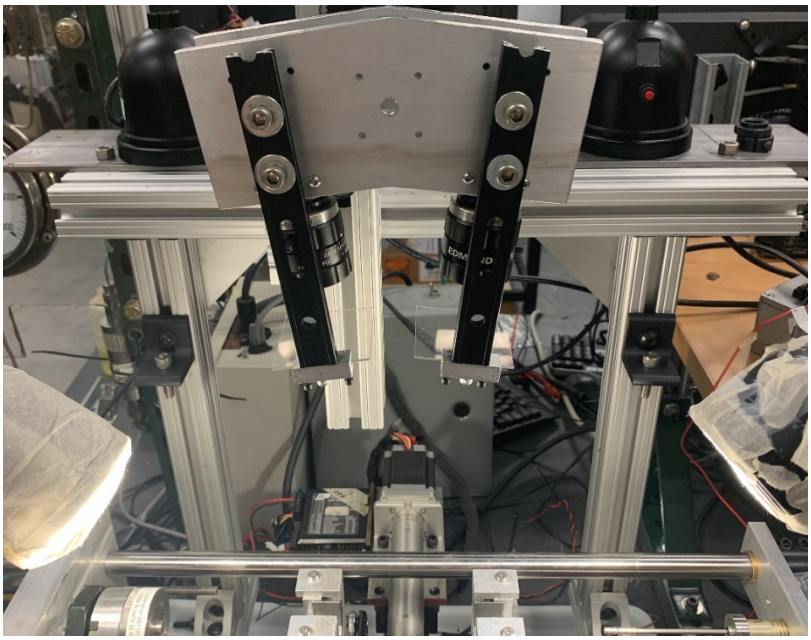

Figure 1.6, 3D-DIC camera setup

The DIC setup in this study involved the use of two angled Point Grey TM cameras with Edmunds Optics adjustable focus lenses in an adjustable rig above the testing rig, shown in Figure 1.6. This setup also included adjustable lighting in order to produce good results for the camera settings and sample speckle pattern contrast, as the DIC imaging process worked by capturing the speckle points and tracking their movement as time went on. When setting up a sample for a test, a high contrast black/white speckle pattern is applied at the end to be used in DIC imaging. This pattern uses a black base coat of paint, followed by a white speckle coat using special techniques. This speckle coat provides a good basis for measuring the DIC strain and other DIC properties for the sample, and can be seen in figure 1.7.

Figure 1.7, DIC speckle pattern

Using the speckle pattern on the sample, the DIC can track the displacement of the sample pattern. In order to read the pattern properly and create a trackable image, the camera system must be calibrated first in order for correct measurement. Before a sample was tested, the calibration would be checked to see if it fell under satisfactory values for error. Once it was found that they were under the threshold, the sample would be run

normally. If not, the camera system would be calibrated using a pre-printed target specimen that the software tracks and analyzes. Once complete, the calibration would be saved, and the camera would be kept untouched in order to maintain the calibration and ensure no tiny movements of the camera. Because of small movements over time, the calibration would still need to be performed often.

1.6 XCT Imaging Technique

The last instrumentation setup used in this study was the use of a XCT Xray machine to scan samples after testing. In previous studies conducted, such as by Yang Chen et al, and by Yuan Chai et al, in situ XCT imaging as a means of measurement has been shown to be a promising method for sample analysis [20, 21]. In these studies, tensile loading with XCT scanning and torsion loading with XCT scanning were carried out. This allowed for sample damage characterization and viewing, giving a better picture of sample failure methods. The method of XCT scanning of the SiC grade cladding to show damage is shown to be promising, and it was utilized in this study as well, albeit in post-processing instead of in-situ. The type of imaging used in this study is consistent with some tests that have used the method as an in-situ test setup as seen before, but the setup and machine used in this study were not able to be combined, so the XCT imaging could only be used as a post-processing tool. After scanned, images would be touched up and edited in order to highlight material trends and notable influences from the failure method of the sample and the loading method applied. The setup for the XCT imaging machine can be seen on figure 1.8.

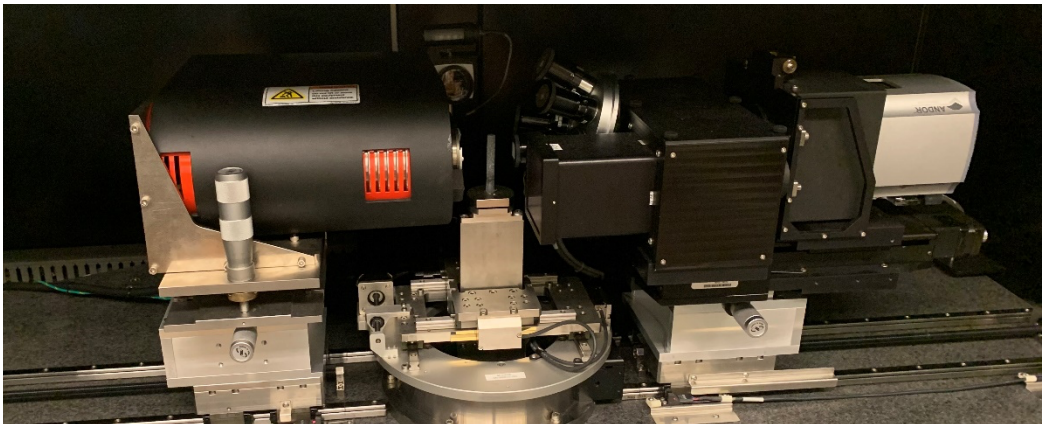

Figure 1.8, XCT scanning setup

1.7 Failure Envelope/Profile

To quantify and explain the entire body of work regarding the results of the tests, multiple methods were looked at as a way to characterize the results. In materials mechanics terms, there are multiple failure criteria that can begin to describe an predict failure behavior in a material. There are cases for ductile, brittle, and composite materials. In the case of the SiC cladding material, ductile failure methods cannot necessarily be used for characterizing it, nor can brittle failure methods. Because of this, failure criteria for composite materials has also been developed in order to make a model in which to fit a composite material and predict its failure. Some of these failure criteria can loosely fit samples of this type, but due to the complex nature and variation in these types of samples, it can be hard to make a mathematical model based on strength parameters to predict this from each sample architecture. In the case of a single ply of a composite, or multiple plies, failure can be found using the first ply failure method, but the complex nature of the sample architecture makes it hard for the samples to match a simple model. In the case of the Tsai-Wu failure model, a model which is often used for composites, a rough calculation can be

done to attempt to fit a failure criteria profile to a set of samples based on architecture. However, again due to the complex nature of these samples it can be more challenging.

In many cases, FEM models to simulate failure for these types of materials can be made for a normal architecture and a cladding architecture. In previous studies, various failure models have been simulated, or applied to the SiC cladding model. There have been instances and possibilities explored with simulating SiC cladding failure in FEM models, as was done in a study by Avincola et al, where the situations of reactor failure scenarios was applied to the cladding to see stress-strain reactions [22]. The failure probabilities in this case were assessed, and a basic analysis of the failure reactions as time increased for the boundary conditions. Failure probabilities are not a newly studied characterization, as can be seen in the study by Stone as well [23]. In another separate study, the modeling capabilities pertaining to unit cells of a triaxially braided composite material are explored, showing that the field of FEA/FEM analysis and prediction for the SiC cladding material is a possibility that can be explored in the future as well [24]. Regarding the theoretical failure of SiC cladding, multiple studies have been done to explore this, or use it as a descriptor in post analysis. In the study by Shapavalov, a basic Tsai-Wu failure map was developed according to the results of the samples and testing, and according to previous material data found from other studies regarding the tow strength and other properties [1]. In with this method, although Tsai-Wu method can be a viable method to analyze sample failure for more simple types of SiC samples and fit it to a model, due to the complex failure behavior with a material that consists of more complexity than a general material characterized by Tsai-Wu criterion, it was seen as a very complex process to attempt to have a true fit to this nature of sample and architecture for the time being. Because of this,

efforts were to focus on trying to create an empirical model for failure that could be applied to this specific type and case of samples, as well as introduce and refine methods for applying multiple failure conditions to these types of sample in a streamlined way. Once all of the tests were carried out and completed, a basic failure envelope graph was created to empirically compare the results and failure strengths of all the tests together. This involved the use of data processing in order to calculate stress and strain relations, and by using the various measurement methods in the test procedure in order to verify proper principal stress load angles as well as mathematically calculate them. By using a graphical representation, the results could be easily compared, and a relationship between failure strengths can be seen. By setting the Y-axis as 90° principal stress angle, and the X-axis as 0° principal stress angle, relative to hoop loading, the framework for a basic failure criteria graph for this batch set of samples can slowly be created. This concept can be seen in figure 1.8.

The key area to address are the parts of the first quadrant in between both axes to the 45° mark. These spots are filled in by the testing of multiaxial failure conditions and modes. As can be seen, the middle 45° line is the case of pure torsion, and the 0° and 90° cases are internal pressure/burst and tension/axial respectively. The combination of these two methods with the torsion method allow for the 90°-45° and 45°-0° ranges to be filled up, depending on the ratios of loading used for each sample. This gives a more clear picture to the behaviors of the material when subjected to multiaxial loading, and illustrates any behaviors to be further analyzed. In this graph concept, the degree mark from the X axis to the Y axis indicates the angle of loading in the sample as is measured by stress calculation, and loosely verified by the DIC imaging process. The distance from the origin to the point

along any degree line on the graph is a representation of the principal stress in that direction, and how strong the material is in that direction. This allows for good comparison between different loading methods in practice, as the difference in strength can be shown as well as the difference in angle, allowing for a easily comparable result.

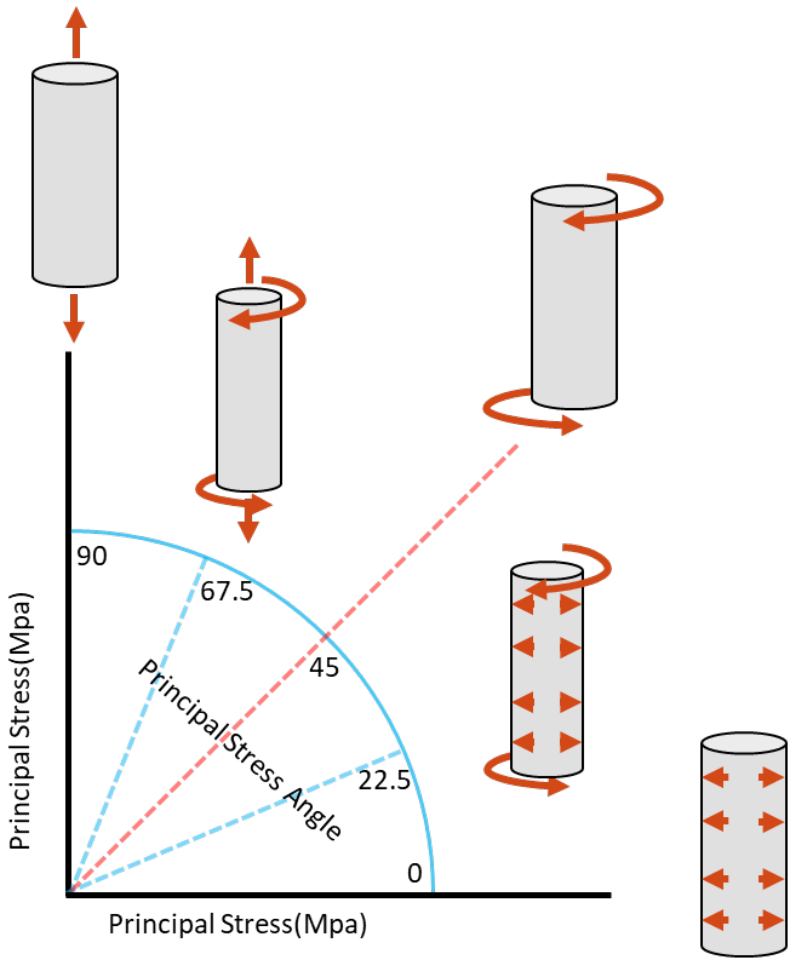

Figure 1.9, Principal stress failure profile concept

CHAPTER 2. LOADING AND EXPERIMENT CONDITIONS

2.1 Measurement and Sample Preparation

In order to characterize the samples and carry out tests on them, techniques of measurement and sample preparation are of large importance to ensure consistency. The base SiC_f/SiC_m cladding samples arrive in 9-12 inch length cylindrical tubes, premade by General Atomics. These samples are cut into various lengths for testing, varying from 2.5 to 3.5 inch cuts depending on test type. The samples are cut using a precision water cooled diamond sawblade, using extra care and time to ensure as little sample damage as possible with a clean cut. Samples would be cut and measured by batch of tubes, as sample tubes could only produce 3-4 cuts of useable sample due to initial size. Samples of the same single full cut of tubing were generally used in the same types of tests if possible. Because of the inexact nature of the length of the base tubing, a test plan was carried out to cut as little sample as possible to generate the required amount of samples, for the sake of efficiency and having samples later on to work with for future testing. This resulted in 2.5 inch cuts for burst samples, 3 inch cuts for both torsion and tension tests, and 3.5 inch cuts for the combined loading methods of tension-torsion and torsion-burst. These cut samples would then be cleaned using acetone and wipes in order to remove any random surface blemishes or debris that ended up on the sample, and to allow for clean placement of strain gauges later on.

Figure 2.1, Post-cut sample

The reasoning for sample length is due to the nature of the measurement techniques, strain measurement and DIC measurement. Because of the amount of strain gauges used as well as the DIC speckle pattern used, these samples needed enough space to have all assorted gauges on the sample. Due to this, the multiaxial combined loading samples had the longest length. These samples were measured using calipers and inner diameter expanding calipers, with a process of measuring at least 6 times each feature on a sample on both sides of the cut. The samples were measured after cutting, before assembly with adapter and gauges. After cutting and measurement, the next step in the process was the machining of the adapters used on the ends of the samples. 3 general adapter types were created and used in this test, with the burst-torsion and burst adapters being the same adapter, the torsion-only adapter being a separate adapter, and the tension-torsion and tension adapter being the same design. In the case of the two adapters with shared tests, the adapter length was changed based on the length of the sample in order to meet a general ~6 inch total length requirement to fit the all-purpose testing rig used. However, outside of that they were identical in geometry but changed sample to sample based on sample measurements. The adapters consisted of a section for sample bonding, utilizing a drill

cutout of roughly 15-20 hundredths of an inch larger than the sample OD, allowing for the sample to fit inside the adapter. The extra room was for the JB Weld epoxy used for setting the samples, ensuring enough space but not too much space for the sample to move before setting.

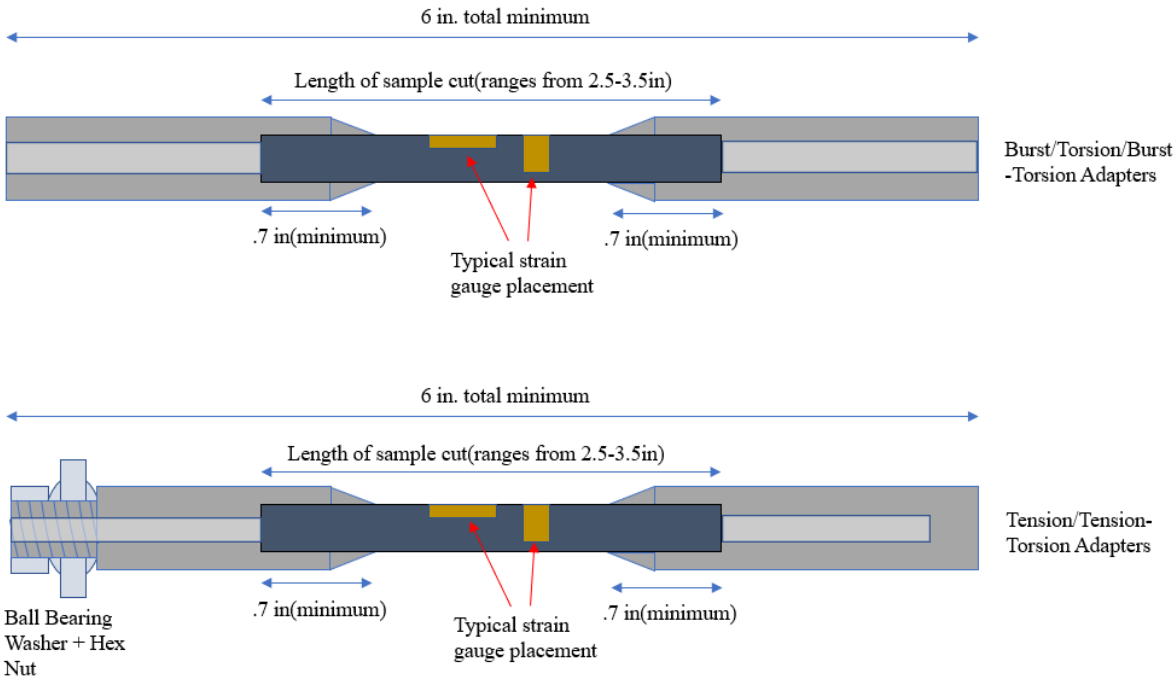

Figure 2.2, Sample adapter diagrams

The JB weld was key in making sure that samples would be able to be secure to the adapters, and to ensure that the sample failed before any part of the adapter or epoxy setup would fail. The samples are then placed in a 120° V-block clamp holder, with shims measured and placed to hold the sample floating in what was the center axis of the adapters. This allows the samples to cure and be properly set for testing and later loading operations.

Once the sample setting has occurred, strain gauges and DIC speckling pattern can be applied to the samples.

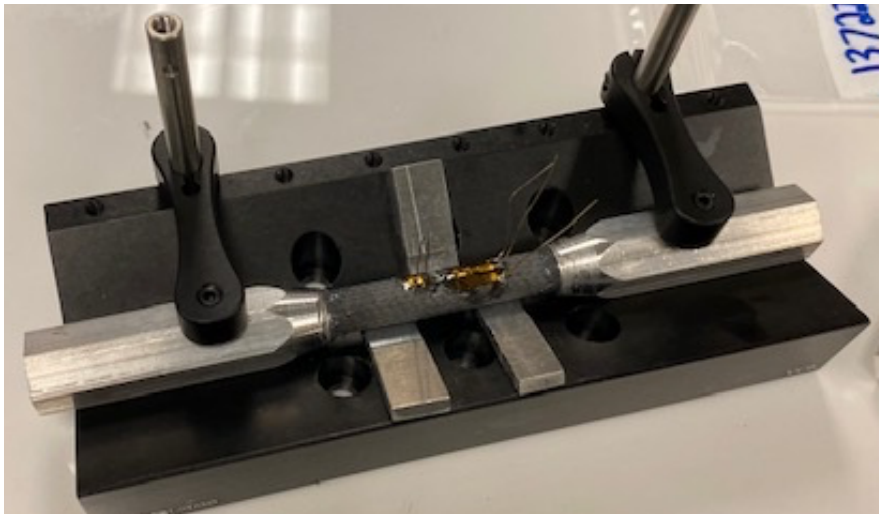

Figure 2.3, 120° V-block alignment setup

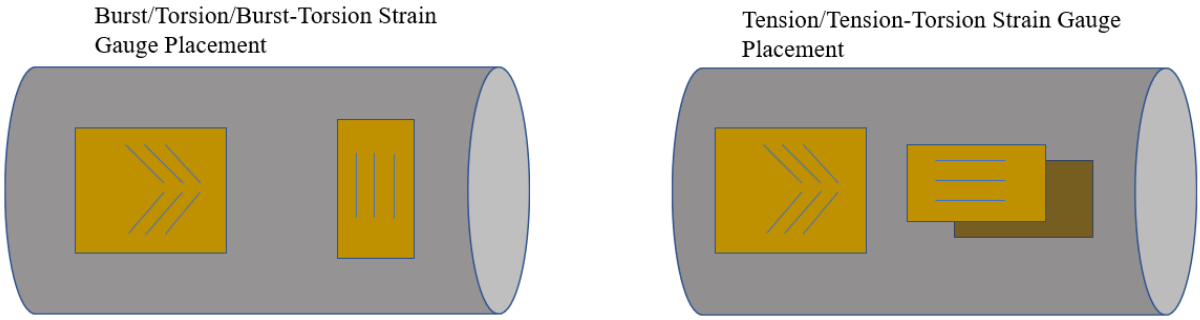

Figure 2.4, Strain gauge layout on tubular sample

Strain gauges are applied to the samples in the orientation needed for the specific loading condition being tested, and once these have cured after around 30 minutes to an hour, DIC speckle pattern can be applied. After DIC speckling, the sample is ready to be

placed on the testing rig. Once placed on the testing rig, AE sensors are attached using hot melt glue and tape to ensure a firm connection to the sample wall. After this is completed, the test is ready to be ran and the sample load data, DIC data, and AE can be processed, and the sample scanned using XCT scanning to see failure modes and close up imaging.

2.2 Burst/Hoop Loading Test

To start on loading conditions, the first type of sample loading considered in this thesis is the hoop loading by use of internal pressure. By internally pressurizing a tubular sample, one can obtain a condition where the sample wants to split open from the inside, which causes a principal stress direction that is 90° from a samples axial direction. In the case of SiC_f/SiC_m cladding, the tubular nature of the sample allows for this test, which has been developed after years of prior testing of different internal pressure tests. In a previous study done in this research group, multiple types of internal pressure loading were performed to compare results and form a similar failure profile, but only with torsion and hoop methods individually [1] In this study, both closed ends and open ended pressure burst testing was performed, along with elastomer plug testing. Some of the previous pressure tests on samples include elastomer plug tests, show in Jacobsen et al [25], and C ring testing, also shown in the same study. In C-ring testing, a cutout piece of material in the shape of a C is pressed down upon in order to induce the same loading condition as pressing from the inside. This is because in an internal pressure test, the internal surface of the material takes on a compressive stress, while the outer surface exhibits a tensile response. By doing a C-ring test, this can be copied to have the same stress response. In an elastomer plug test, the use of an internal plug which can expand under certain conditions, such as applying an axial force to the plug and compressing it to the sides. This expansion

results in an internally applied stress to the outer tubular sample. These tests are some of the previous methods used, but the one focused and developed for this test was the open end burst pressure test. Through some of the development from the previous work of Shapovalov's method of internal pressure testing, the method through which we run the tests was created and expanded upon [1].

The method and theory behind the internal pressure method revolves around the thick walled pressure vessel equation, an equation known as Lame's equation. This equation is below:

$$\sigma_\theta = \frac{r_i^2 P_i - r_o^2 P_o}{\left(r_o^2 - r_i^2\right)} + \frac{\left(P_i - P_o\right) r_i^2 r_o^2}{\left(r_o^2 - r_i^2\right) r^2}$$

Eq. 2.1, Lame's thick wall pressure equation

This equation can be further solved down, with the parameters of only applied internal pressure, and at the outer surface of the material, to get the hoop stress of the sample/test. By setting the outside pressure to atmospheric pressure, it is unchanged and can be solved out of the equation, resulting in the simplified equation for hoop stress at the outside surface, ($r = r_o$):

$$\sigma_\theta = \left[\frac{2 P_i r_i^2}{r_o^2 - r_i^2}\right]$$

Eq. 2.2, Simplified int. pressure stress equation

Using this equation, the hoop stress of the material can be found. By combining this with the previously mentioned strain capturing techniques, a simple stress strain curve for the material can be created. By utilizing the stress and strain of the material as well as the AE analysis data and DIC measurement data, the PLS and UTS values, as well as verification of the principal load angles of stress, can be found for the internal pressure test.

The internal burst pressure test is ran by utilization of a hydraulic crank pump, which delivers oil through a pipe assembly.

Figure 2.5, Pressure gauge assembly

In the assembly, there is a pressure gauge as well as turn off and relief valves for the sake of safety and depressurizing if needed. The pressure is also recorded by the DAQ, which can later be used for stress processing to calculate. The assembly of the pressure rig and pressure control pump leads to an adapter on the sample, which is attached to the sample by a specially made high pressure seal attachment, and this seal assembly can be moved and clamped down along a set of guide rails that control where the sample and testing rig line up. The guide rail setup developed is an initial design from previous research group work, and it was developed and refined for later use with all 5 testing methods used in this study. The main changing parts on the rig are the high pressure seals that slide to fit outside of the samples, which would be changed out for the tensile load cell referenced later in this study. The bladder assembly works by sealing off the sample and enabling a pressurization from the pump to past the end of the sample, ensuring a uniform pressure load from the inside of the sample. This pressure loading scenario can be described by the below graphic:

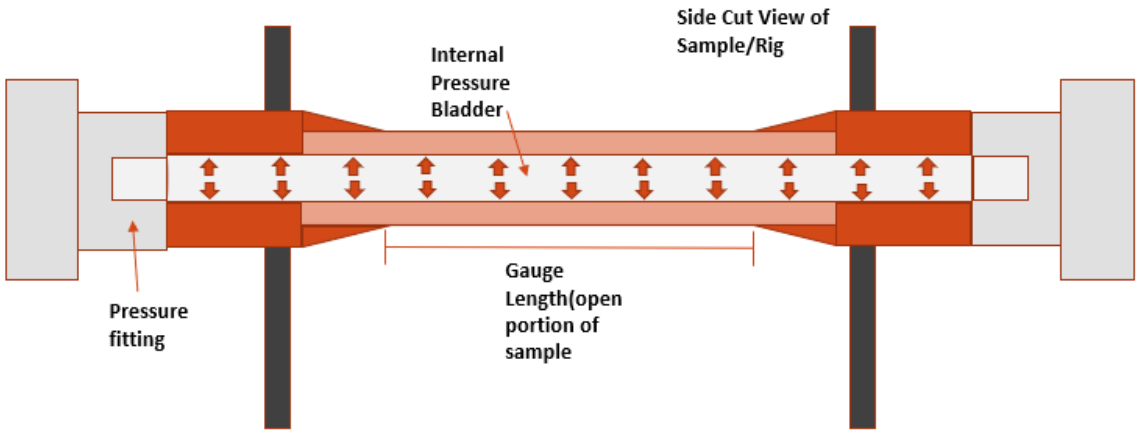

Figure 2.6 Internal pressure rig application

The internal bladder, which in this case is round plastic pressure tubing, expands to the inside of the sample, applying an internal pressure. This allows for the sample to have a hoop stress applied on the outside of the sample. To prepare samples for this type of test, the process involves taking a tubular sample of SiC_f/SiC_m cladding, provided by General Atomics, and attaching it to specially machined hex adapters made in house for this type of sample. These adapters allow for secure snug placement into the testing rig, and allow for further applications of torsion if desired for different types of testing. The burst and torsion adapters are made the same way, allowing for easy repeated testing and quick turnaround for making adapters for the samples. Once all the necessary sample preparations are done for a burst sample, it is ready to be tested. The internal pressure method has been previously verified in the study by Shapovalov when the method was developed, so the only verification of the method needed is the combined burst-torsion loading method [1].

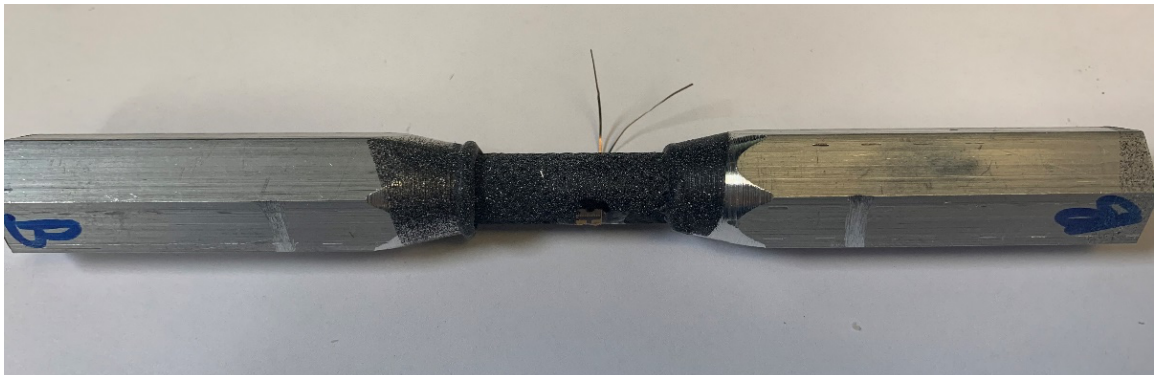

Figure 2.7, Internal pressure “burst” sample

2.3 Axial/Tension Loading Test

The next loading condition addressed in this study is the axial/tensile loading condition. This loading condition is a type of test that is well developed in most cases, utilizing some variants of standard motion/displacement controlled grip machines to carry out tensile tests that grip both ends of a sample, generally a shaped plate of the material that fits whichever type of grip used. In this type of test, an axial force in tension is delivered to the sample by pulling these grips apart. Previous testing on SiC matrix composite material has been carried out in the generic method mentioned above, with methods even being used with in-situ tests for the purpose of tomography scanning, such as in Chen et al [18], or for the sake of verifying the material strength and matrix cracking patterns of different combinations of SiC architecture and composition through use of tensile testing, shown in a study by Morscher et al [26]. This process was not done on cladding shaped material in both cases, however, but the damage and cracking exhibited in these types of samples can still be useful for comparison. In the case of SiC_f/SiC_m cladding, this gripping of the sample can at times be challenging due to the brittleness of the material, as well as shape, causing small amounts of damage before loading the test, and also small amounts of off center loading and unwanted bending in the sample. Studies previously carried out by this research group had used/considered the use of the normal testing method for axial/tensile testing of this cladding, seen in Shapovalov et al [1] via use of a General Atomics test setup using such a machine. This is a similar setup to testing done in Deck et all [8], with use of grips and epoxy on cladding samples as well as special loading joints at the machine interface to allow for as little off center loading as possible. These tests were run in accordance with ATSM standard C1773 [27] which denotes the general process for

tensile testing on these types of samples. The loading method used in this study differs greatly. The method developed in this test utilized an internal push rod, which runs inside of the sample, and gives the test rig the capability to induce tensile force on the samples. The basis of this new method is the use of special adapters on the sample, which utilize certain behaviors to attempt to center the material as the test is ran in the axial direction using this push rod technique.

The basis of axial testing is basic stress mechanics, as it has been studied extensively that applying a tensile force to stretch a material is a proven method to measure its material strength. The basis for this calculation and method lie in the simple stress equation based on cross sectional area:

$$\sigma = \frac{F_n}{A}$$

Equation 2.3, Tensile/compressive stress equation

Using this equation, the tensile or compressive stress of an object can be found. The force acting in the direction normal to a plane cutout of the middle of the material is denoted as Fn, whereas the area it acts over is denoted as A. Using this and the cross sectional area of the cladding material samples after measurement, the tensile stress of the sample can be calculated by taking the applied load divided by the cross sectional area, which is calculated by using the ID and OD of the sample. In the case of our tensile testing, the load reading from a load cell used in testing to apply the tensile force is converted into the proper unit and calculated into the tensile stress exhibited on the sample.

The internal push rod method described earlier in this section is broken down into two portions. The load cell application, and the delivery to the sample. Anchoring the sample while using the push rod creates a tensile effect. The left side of figure 2.9 is the side that is anchored, specifically against one of the testing rig's baseplates. On the opposite side of the sample, the free floating baseplate can have a friction force result from the tension applied to the sample. Because of this, the bending of the plate due to tension is factored into the full stress calculation of the sample. The push rod that is utilized is a precision ground .25 inch rod, with both ends ground for flatness. The load cell mentioned previously is moved by used of the same hydraulic pump used in the burst testing, attached to a different loading mechanism that turns the pressure applied into displacement of the load cell. This load cell contacts the push rod at as close to the direct center as possible, and in line with the line of loading along the test rig. The center line of the test rig was measured and set before testing to ensure accuracy. By use of this load cell to apply direct force, the calculation from it is fairly easy from the data received. The load cell is anchored by threaded rods to the left baseplate in Figure 2.8, which is the baseplate that receives the force of tension from the sample.

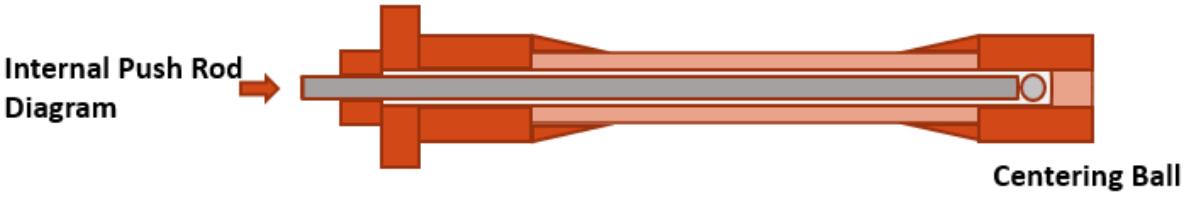

Figure 2.8, Internal push rod tensile method

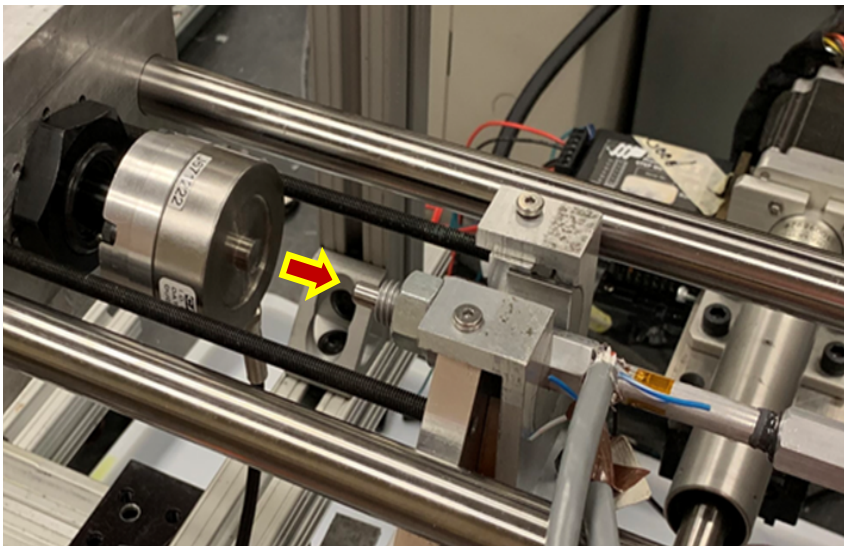

Figure 2.9, Load cell push rod contact

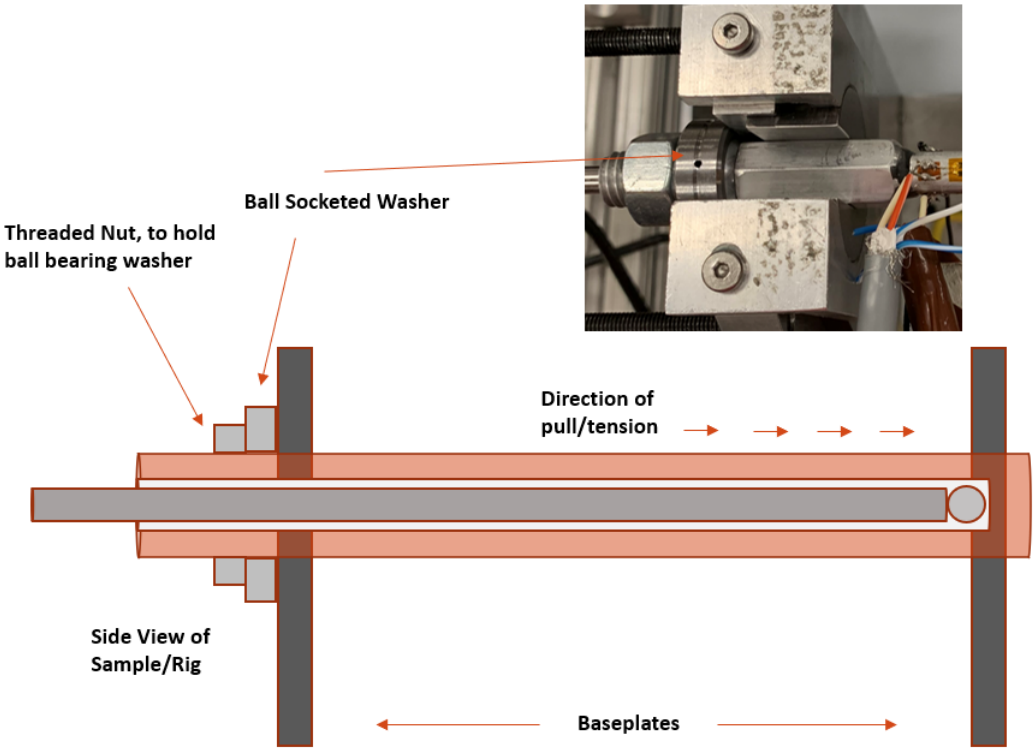

Figure 2.10, Internal push rod diagram

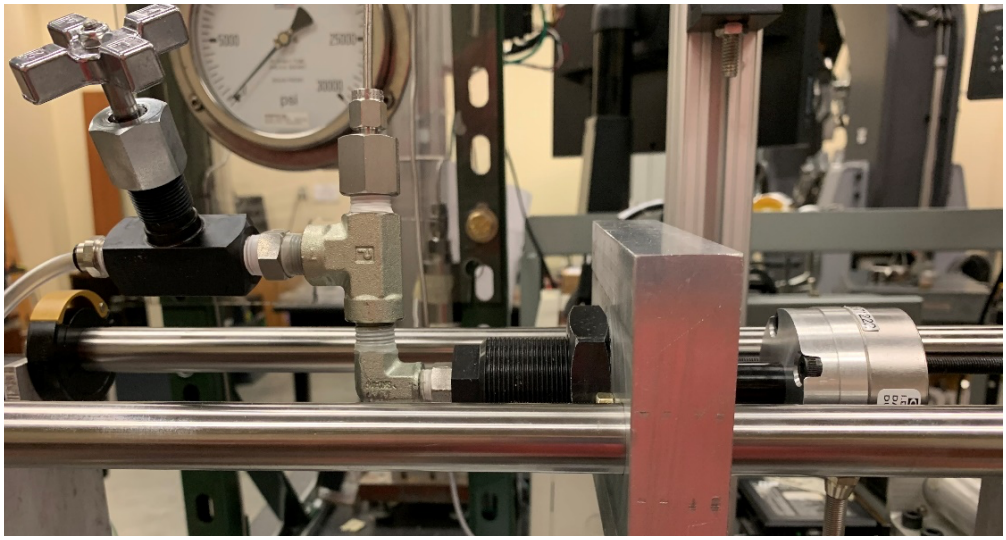

Figure 2.11, Hydraulic actuator with load cell mounted

The adapters used in this type of testing involved two different adapter side designs, one side making use of a ball bearing washer held in place by a bolt, machined to ensure a snug and flush fit on the sample, and the second side, containing an internal slot for a .25in precision ground steel ball which sat in the adapter in the center of axis. The entire adapter had a drilled hole measuring minimally higher than 0.25in to allow for the push rod to pass through securely with minimal side to side movement if any. Images of a typical tension adapter and sample combo is included for reference to help describe the device.

This entire process creates a tensile force on the sample, which was verified through a similar verification process as the burst test. A dummy aluminum sample was created to simulate testing parameters used in a real test, and loaded accordingly. The key finding in verifying the aluminum sample was that use of at least 2 tensile strain gauges is necessary for this type of test in order to ensure accuracy. By using 2 or 3 tensile strain gauges, the tensile strain induced could be averaged to find the true strain in any case of slight off

center loading. In the dummy test using 3 strain gauges, using a similar sample size of 0.272in ID and 0.375in OD, it was found that the elastic modulus of this aluminum sample averaged 67.5 GPa, right around the values found for aluminum. Using this method and process, the torsional loading rig on which the test rig is based on could be used for both tension, torsion, internal pressure, and the 2 combined methods included in this study. Different dummy samples were used for the testing scenarios in order to verify the testing conditions. A setup of this verification sample is included in image 2.11 to also show the setup of the testing rig and it's use.

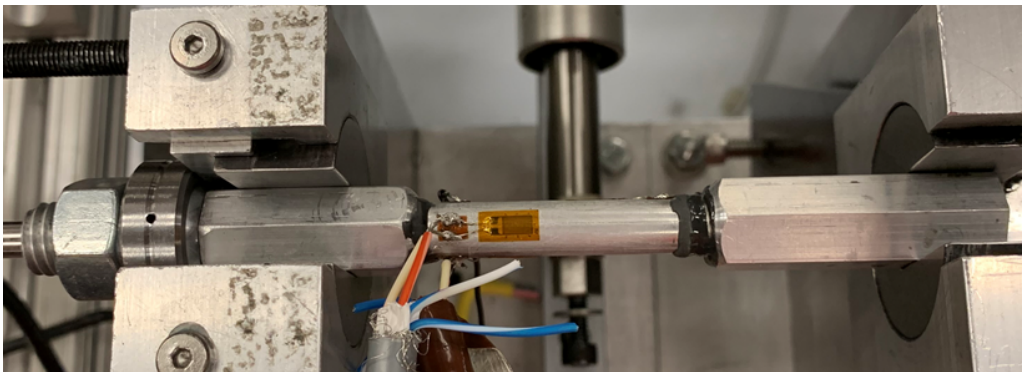

Figure 2.12, Tension dummy sample with tension adapters

2.4 Torsion Loading Test

The final uniaxial loading test utilized in this study was the torsional loading of the SiC_f/SiC_m samples. The torsional loading of a tube/cylinder is a very well developed type of test, and there are many examples to go off of in basing the method. In the case of a hollow shaft in torsional loading, the general equation for calculating torsional shear stress, which is the metric sought after, is as follows:

$$\tau = T * r / J$$

Eq. 2.4, Shear stress(τ) in a twisting shaft

This equation utilizes the applied torque, the radius or distance from the axis of rotation to the stressed surface, and the polar moment of inertia of the shaft in order to determine the stress. The torque resulting from a force applied a distance away from the shaft, and the polar moment of inertia for a hollow shaft, are calculated using equations 2.5 and 2.6 as follows.

$$T = F * d$$

Eq. 2.5, Torque equation

$$J = \frac{\pi(D^4 - d^4)}{32}$$

Eq. 2.6, Polar moment of inertia for circular hollow shaft

Using all 3 of the previous equations, the torque and shear stress of a circular hollow shaft can be found from calculations using parameters measured in a testing environment. This is the basis for a torsion test on a circular tube of any type. In regards to SiC_f/SiC_m cladding tubing, torsion testing is a method that is used to test material strength. The application of shear stress to a cladding specimen using torsion methods is useful in order to find information surrounding the material strength, as in SiC_f/SiC_m cladding tubing, fiber

direction angles can have an effect on material strength, and torsional loading allows for a loading scenario that can be closer in principal stress loading angle to the sets of fibers that run in directions at an angle from the axial direction. Different methods of carrying out torsional tests have been developed over the years. In a study by P. Potluri carried out on biaxially and triaxially braided composite tube samples, similar to the triaxially braided SiC_f/SiC_m samples in this study, use of a Instron machine attached to a rotating chuck was used to induce torsion on samples in a controlled manner [28]. This is similar but not the same to the method developed in this study, in that the method in this study also requires use of a linear control to apply a rotating torque. However, this idea of using a linear control is different from some types of testing using the rotation capabilities of some models of grip tensile machines such as in the study by Bernachy-Barbe et al [2]. In a study done by this research group in Shapovalov [1], the basis for a torsion rig which this study also expanded upon was introduced. This torsional rig used simple hex wrench adapters combined with a linear motor to induce torsional loading on a sample. The expanded version of this testing rig is what was used in this study, with a focus on refining the method and adding additional testing parameters such as the already developed internal pressure method and the newly introduced tension push rod method. New studies in the field have also adopted use of torsional in situ loading and damage characterization by use of XCT scanning, which is a capability that was not explored in this study, but similarities in the reaction of the material to torsional loading were considered [21].

The testing rig that has been developed for torsional loading in this study is an expansion of previous efforts in the research group at USC, and the mechanics behind it are presented in the following information. Using a fixed end and an applied load end, two

hex wrench adapters deliver torque to a sample by use of special hex adapters attached to samples. The fixed end contains a load cell, which can read up to 100lbs of applied load. This setup can be seen in figures 2.13 and 2.14. This torsion application method is useful in that it allows for the extra loading cases previously mentioned, while applying the torque as well. This allows for better efficiency to test samples. The sample adapters made for both the burst and tension tests, can both be easily adapted to include torsional testing in the same test, using two different programs created in house to control load application. The motor controlling the linear applicator attached to the left wrench of figure 2.13 and 2.14 can move in and out by manual in-program control, and by the program operation load control method. This load control is set by itself in the case of torsion only loading, but in the case of both the torsion-burst and tension-torsion testing, the torsion can be driven by the internal pressure load and the applied tensile load respectively. A verification of the torsional loading was done on an aluminum dummy sample as well, and using an aluminum sample in normal sample adapters, a shear modulus of 26.2 GPa was found for the aluminum dummy sample, well within the range for an aluminum alloy.

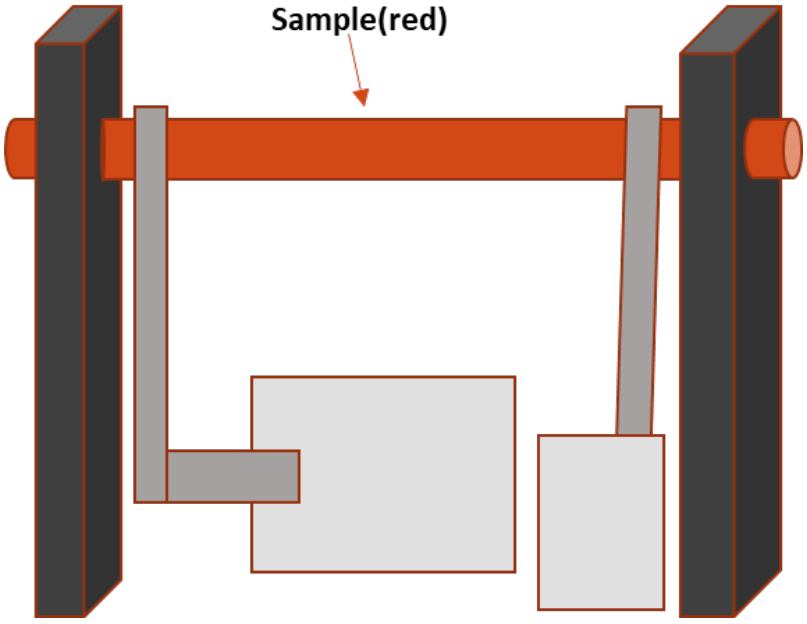

Figure 2.13, Torsional loading method

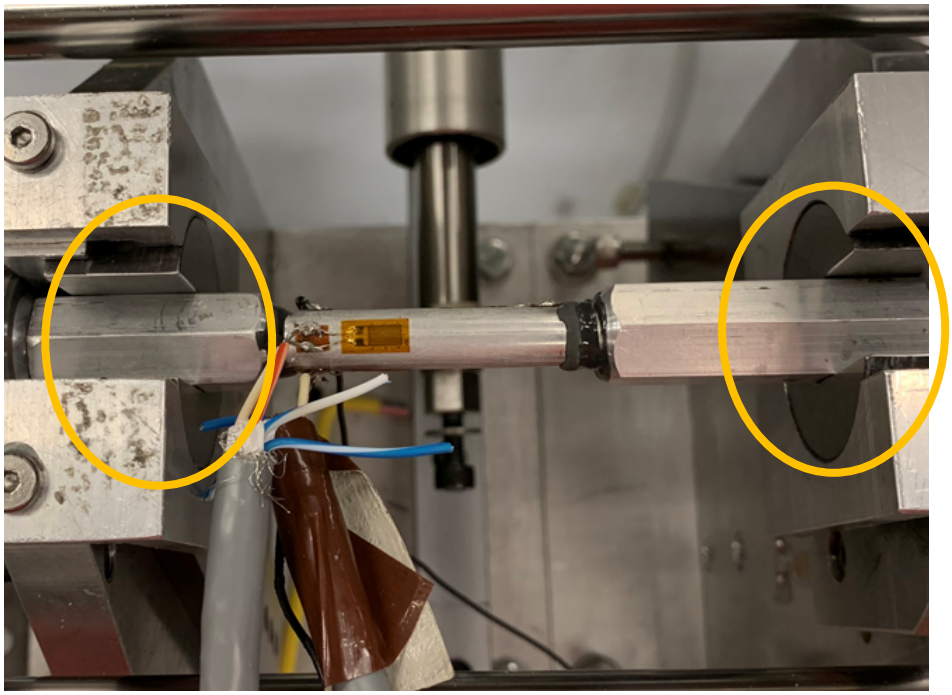

Figure 2.14, Torsional loading hex wrenches

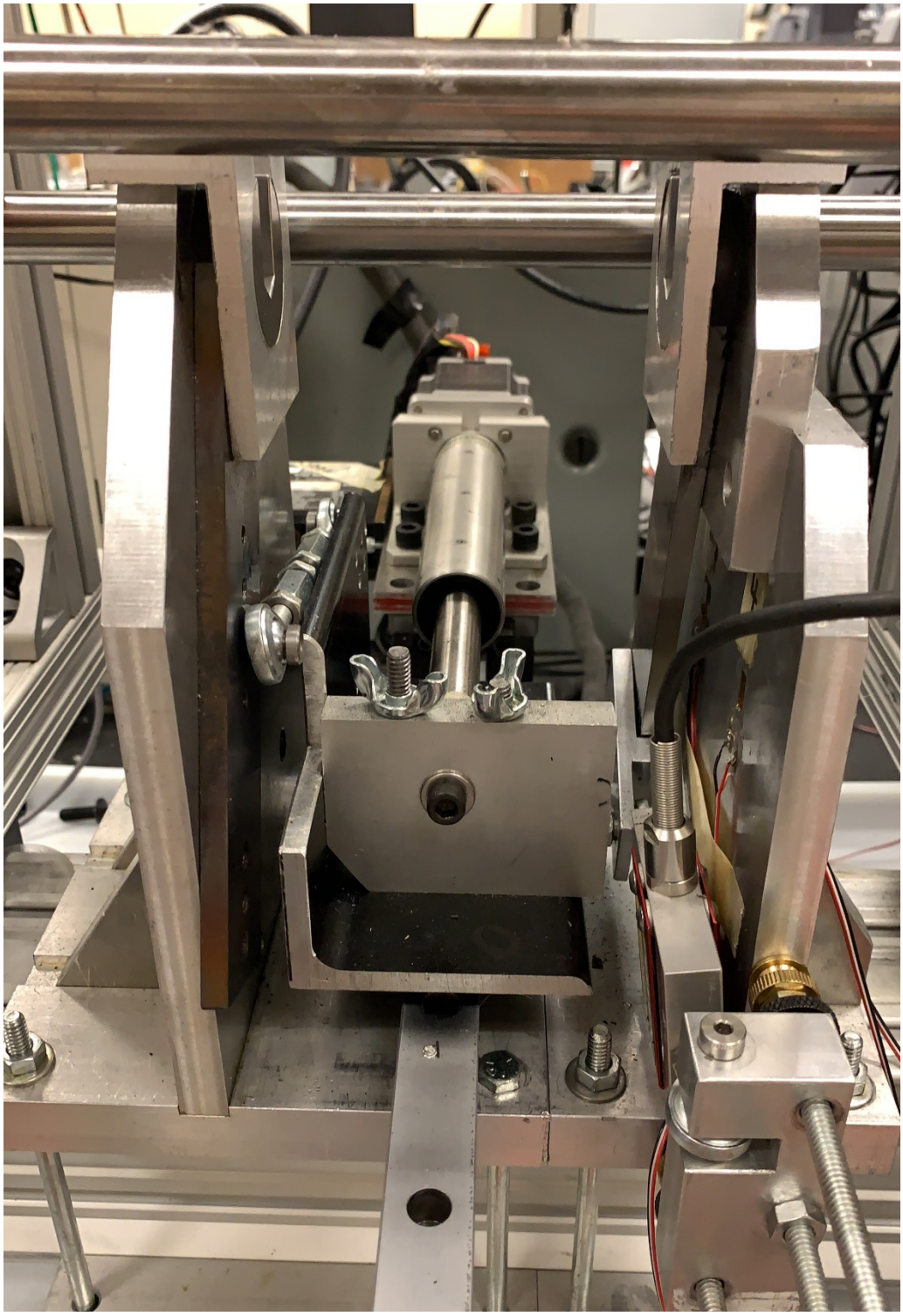

Figure 2.15, Torsion loading frame

2.5 Burst-Torsion Loading Test

The burst-torsion loading method used in this study was developed in house at USC. Using the methods and theory seen in both the internal pressure and torsion methods explained above, the two loading procedures were combined to produce a multiaxial test in which internal pressure loading can be loaded, which can then drive a torsional loading component as a result. In the study mentioned previously by Bernachy-Barbe, the tension and internal pressure methods were combined to produce results regarding multiaxial loading [2]. The loading method used in that study is similar to what was accomplished in this study, but in the case of this study the torsion and internal pressure methods were combined to produce a multiaxial stress-strain response. Outside of that study, the combined method of internal pressure with other loading methods is a generally new type of test for these samples. This torsion-burst combined method opens new possibilities in how a sample of this type and style can be tested with regards to combined hoop strength and shear strength, and the capability to load samples with controlled principal stress load angles. In a general torsion sample, using a 2D stress element for plane stress at a point on the sample, the angle of principal stress can be found to be 45° in pure torsion. In a pure hoop/burst test, the principal stress load angle is 0° in reference to the sample being stood up lengthwise. This can be seen in figure 2.16. As can be seen by the previous figure, in the case of this study, the angle in which the principal stress is applied is 90° when along the length of the samples, and 0° along the width of the sample. In a tension test, the sample is pulled apart and the line on which the force acts is along the 90° direction in the figure. Likewise, in a hoop strength test, the force acts along the 0° line of the sample instead. When the internal pressure and torsion tests are applied together, the load angle of principal

stress can be controlled depending on the ratio between the two loading methods. The angle can be controlled in combined burst-torsion testing anywhere from 0°-45° in theory, allowing for the capability of testing the sample in a variety of different principal stress directions.

Figure 2.16, Principal stress angle on sample

The verification of this method was done by using an aluminum dummy sample, with the hoop and shear stresses and strains calculated out for the sample in a loading cycle. It was attached using the same process with JB Weld and strain gauges, and placed onto the testing rig as shown in figures 2.17 and 2.18.

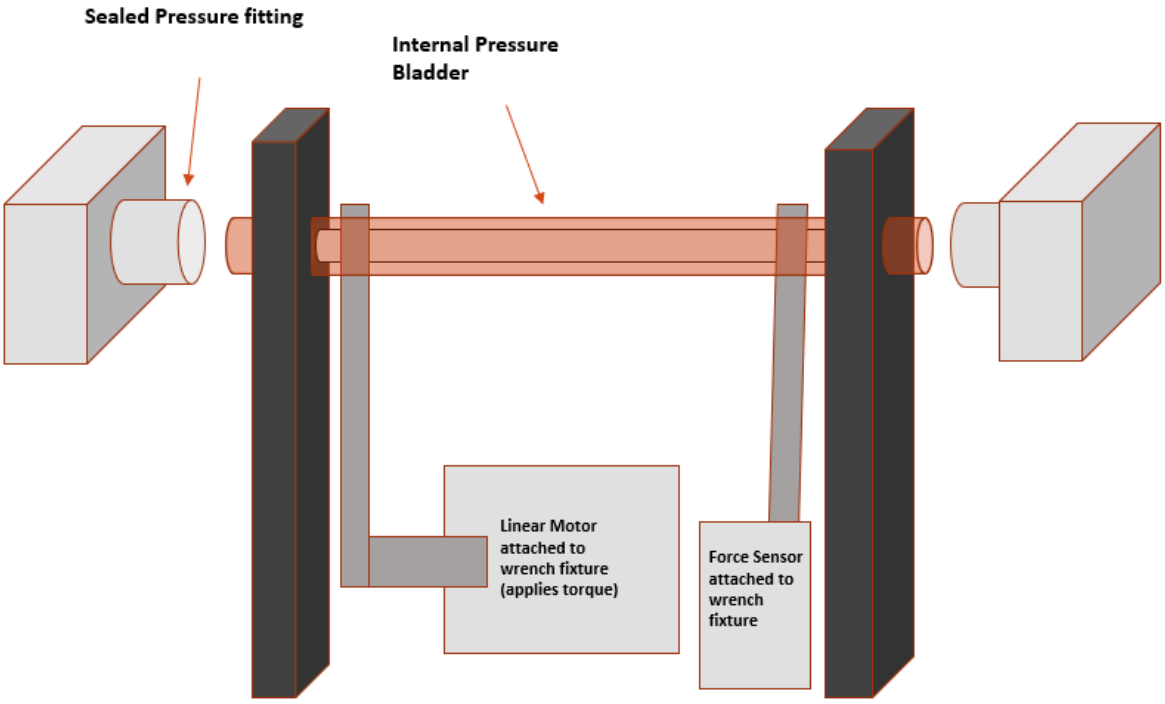

Figure 2.17, Burst-torsion rig configuration

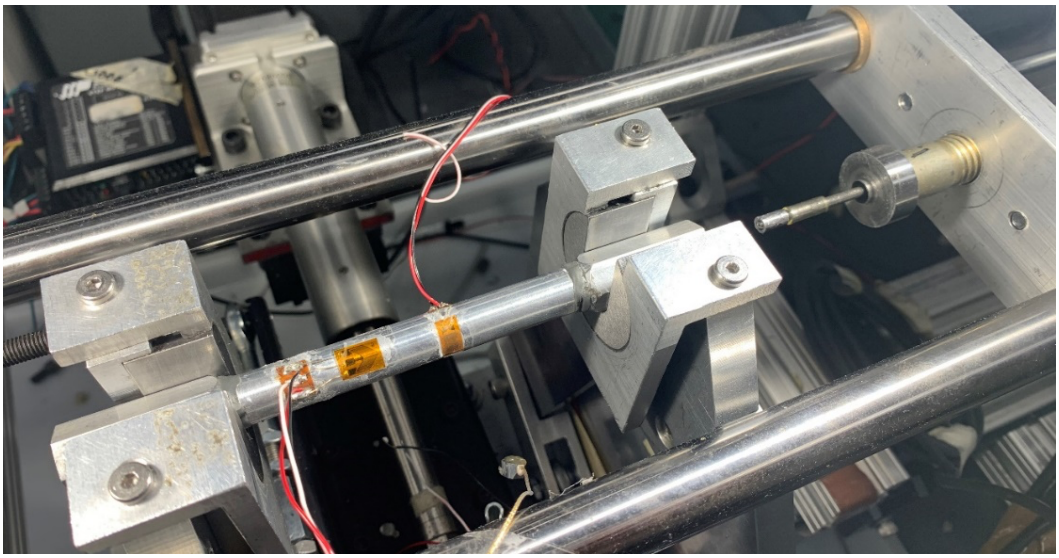

Figure 2.18, Internal pressure and torsion verification test

This dummy aluminum sample was measured to have an ID of 6.55 mm and an OD of 11.938 mm, and loaded to a very small amount using the loading technique for internal pressure and torsion. By loading to a predetermined stress level, the strain was then measured to find a young's modulus and shear modulus for the aluminum sample based on stress-strain relations. This resulted in an Elastic modulus of 67.7 GPa and shear mod of 27.4 GPa. These values fell right around the range for elastic and shear moduli of an aluminum sample, giving reason to believe the internal pressure torsion combined method was producing correct results in practice, and that the method could be used to carry out sample testing. These dummy sample tests were conducted many times to ensure accuracy.

2.6 Tension-Torsion Loading Test

The last loading scenario considered in this study is the tension-torsion test. This type of testing is a well-developed method in regards to the base test itself, with many types of mechanical test machines available for this type of testing. The nature of the tension torsion test is that it usual combines the tensile loading with a torsion loading through the use of a standard MTS tensile machine. Many of these machines have rotating clamps allowing for application of torsional loading as well as the standard tensile component. When it comes to SiC_f/SiC_m cladding samples, there can be challenges in loading the cladding properly to ensure pure tension and torsion loading, and to ensure the material is on axis correctly. Previously, studies have been carried out on tension-torsion of SiC cladding samples. In a similar study involving uniaxial and multiaxial tests, Bernachy performed tension-torsion tests on SiC cladding samples [2]. Their study utilized a more classic setup, using a force controlled tensile loading machine with sample glued in metal adapter [2].

In this study, a new method was developed using the previously mentioned push rod technique and torsion methods. Using a combination of these two effects, the tension torsion test could be ran with the testing rig/setup that had already been created. The previously mentioned basis for both the torsion and tension methods can be considered for this. A new problem that arose from the development of this method came in the form of possible friction as a result of the combined torsion and tension causing applied load to the secondary plate on the testing rig. This problem arose from the difference between the tension-only test and the tension torsion combined test. In the tension only test, the sample can more freely move in the hex clamp on the non-fixed end due to zero applied torque on that hex wrench. This problem was analyzed to find that when a sample was torqued down, and a tensile force was applied, there was a small force bending the opposite plate from where the force was applied. From the application of torque, the sample could no longer move as freely due to friction from the torsion load, and as a result the right hand plate which held the free side of the sample would take on a residual axial force from the testing setup. To mitigate this effect, a full bridge sensitivity bending strain measurement method was used to read the plate bending, and use the measurements of the plate and the plate's strain and properties to calculate what the axial force applied taken on by the plate was. An image of this setup can be seen below, with the reverse side of the plate having the same orientation of 2 strain gauges mirrored.

In testing and verifying this problem, it was found that the plate receives anywhere from 0 up to 15 kg-f in the case of a tension torsion test. This was then factored in to the calculations for axial stress in the case of the tension torsion tests as a reading that is recorded on the same timestamp as the general test. In actual testing, this value represented

around a 6-7 MPa change in stress, so when the gauge is reading a value that would result in a stress of 150 MPa, the actual sample would be experiencing less than that value by a slight amount, which would be calculated to have the real stress value of the sample by subtracting the bending strain load cancelation value.

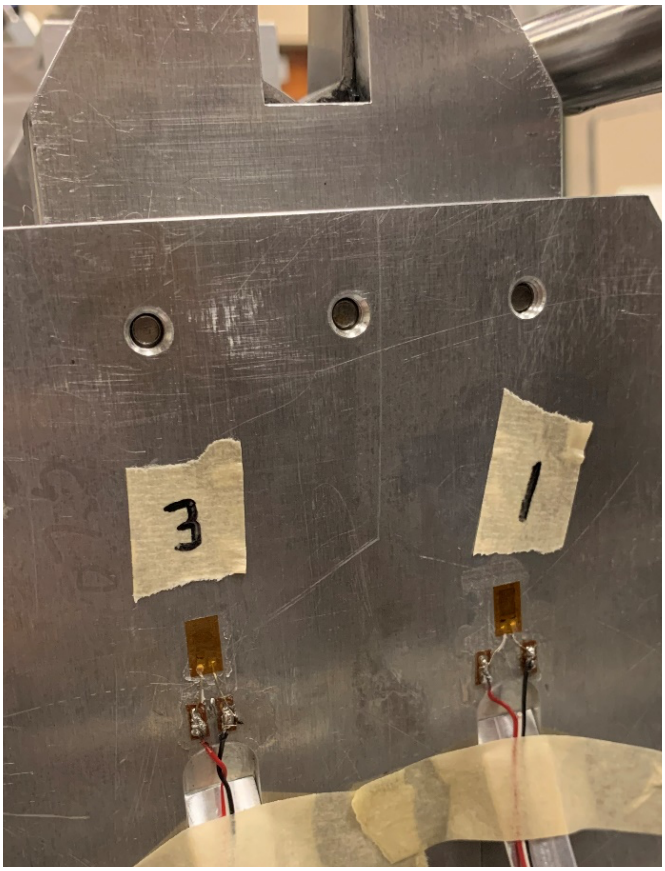

Figure 2.19, Bending strain cancellation setup

The load control on the tension torsion machine was accomplished by use of a similar program compared to the torsion burst combined load test. By switching out the load controlled portion of the test to the manual tension load, the tensile load could be used to control the torsion loading. The manual control on the test would be the applied tensile

load through the load cell applicator, and this signal would read out to the program and cause the torsion load to follow in suit by use of the torsion linear motor and torsion force sensor. The ratio at which these two would follow could be selected in the program off of any calculations made pre-test to find a suitable ratio for the desired failure/principal stress angle on the sample.

Using a dummy aluminum tension-torsion sample on the testing rig, verification tests were carried out in order to make the developed method as accurate and repeatable as possible for the later tests. This verification was done by analyzing the tension results with an applied torsion as well as the bending calculation from the plate previously mentioned. Knowing that the torsion method, tension method, and the torsion burst combined method was already verified, the only thing that needed to be verified for the case of this test was the result of the effect of torsion on a tension sample, and the friction/plate bending that could result from this effect. When tested, it was found the aluminum dummy sample had a young's modulus of 66.5 GPa, with the bending of the plate factored out and the torsion applied to cause the friction problem mentioned previously.

CHAPTER 3. RESULTS AND DISCUSSION

3.1 Burst/Hoop Loading Test

Looking at the results of testing, the first test to address is the burst/hoop/internal pressure test. These samples were prepared using the previously mentioned processes and processed using the measurement methods previously mentioned. The samples had a repeatable failure mode, with an average PLS of 36.87 MPa, and an average failure stress of 129.81 MPa, with a principal stress angle of 0°.

Table 3.1, Burst/hoop sample measurements

Sample #	**ID (mm)**	**OD (mm)**	**A (mm^2)**	**J (mm^4)**
181-1-A	7.607	9.042	18.76	327.55
181-1-B	7.582	9.055	19.24	335.62
181-2-A	7.569	8.992	18.50	319.46
181-2-B	7.557	9.081	19.91	347.38

Table 3.2, Burst/hoop sample stresses and angles

	Principal Stress MPa		**Principal direction (degree)**	
Sample #	**PLS**	**UTS**	**PLS**	**UTS**
181-1-A	37.60	138.33	0°	0°
181-1-B	37.01	135.48	0°	0°
181-2-A	35.22	130.93	0°	0°
181-2-B	37.63	114.49	0°	0°

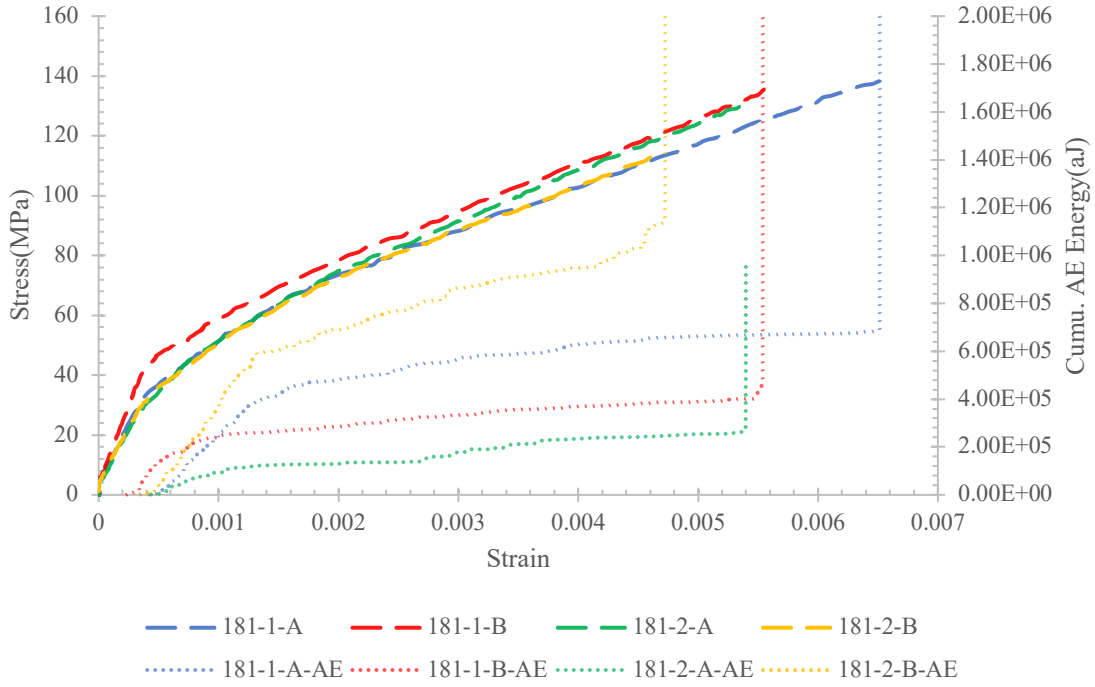

Figure 3.1, Internal pressure/hoop stress-strain, AE results

In Tables 3.1, 3.2, and Figure 3.1 are the individual stress-strain and AE results for the tests. These include all the samples mentioned in the previously mentioned tables.

The AE details and data can vary from sample to sample based on strength of the application/bonding of the sensor to the sample itself, which is why there are variations in the AE signal strength from test to test. However, the strength differences are the same for the entire test, and allow for the comparison of loud events to the loudest event in a test to still be carried out with accuracy, as the data is being compared relative to itself when used to help find PLS.

The next data parameter to look at is the DIC imaging. DIC imaging, as previously mentioned, was used visualize the full-field strain induced on the sample, and can be used to compare localized strain recorded from a strain gauge.

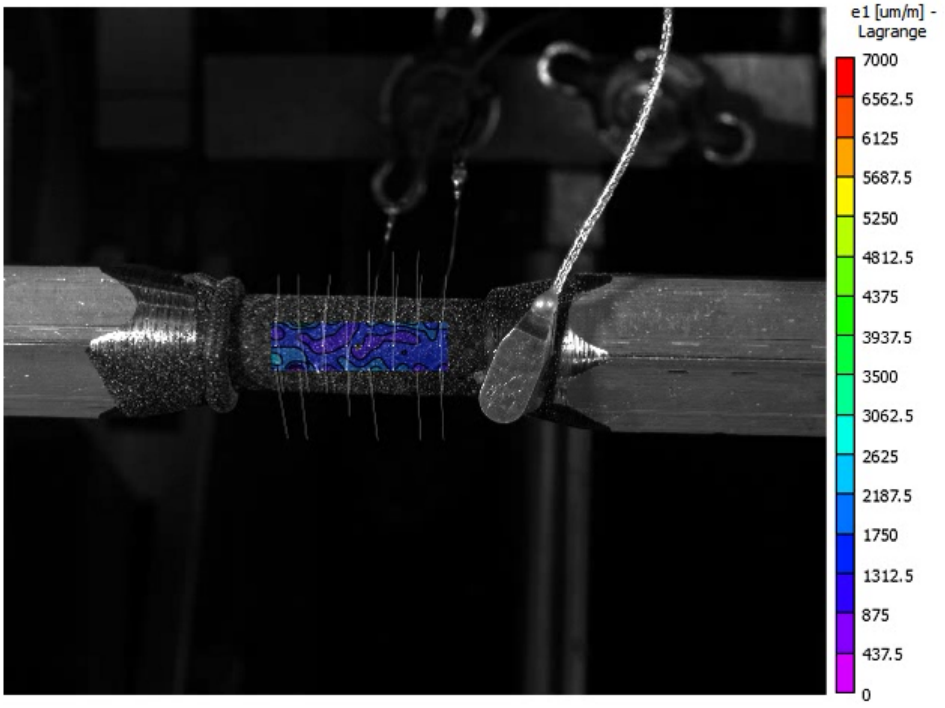

Figure 3.2, Burst test DIC imaging vectors, principal strain(after test start)

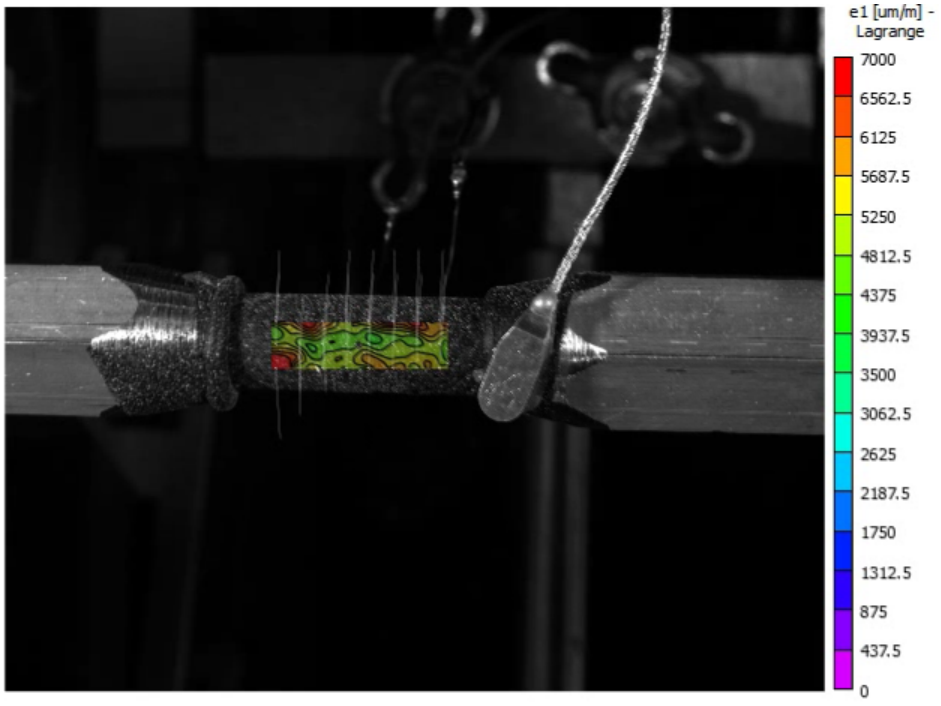

Figure 3.3, Burst test DIC imaging vectors, principal strain(right before failure)

In these DIC images, one taken closer to the beginning of the test, and one taken right before sample failure, the vector lines can be seen to have a straight up and down 90° orientation. This is consistent with all the burst/hoop samples, as the load is applied by the internal pressure pushing the sample apart along the spine of the tubular sample. This can be seen by the strain map's orientation being perpendicular to the loading direction. Although DIC strain measurement is useful to find strain, due to the rough nature of these cladding materials with a curved surface being analyzed by the DIC, the actual strain accuracy in this format can vary slightly compared to what the localized strain gauges read-out on the sample. However, the general trend of loading direction and zones of high damage/strain accumulation can still be seen, and it is a useful tool to analyze these samples.

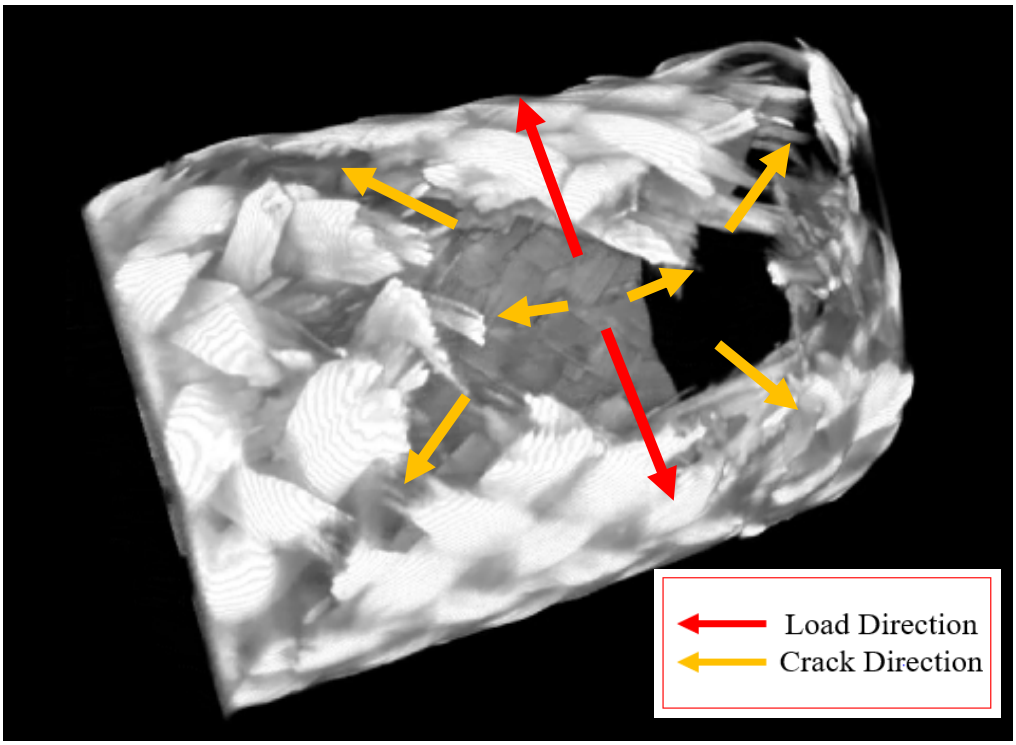

Figure 3.4, Burst/hoop test failure XCT scan

The next step after testing was to analyze the XCT images from the sample after failure, to get a clearer view of the failure mode of the samples. A representative XCT image of an internal pressure/hoop test is included to show the effects of internal pressure on this architecture and batch of samples. This failure mode was very repeatable for this batch of samples and loading condition. It was noticeable that these samples, compared to previous architectures of samples tested, had a failure mode that was more fragmented and less directional along the loading line, as can be seen in the figure 3.4. This failure exhibited a general direction along the load line, but spread out further along braid architecture lines of the sample in the 45°/diagonal direction, showing a weakness towards breaking in that direction. The sample did not have any large pieces of debris fall off when failing, and stayed intact other than the failure location.

3.2 Axial/Tension Loading Test

The second test analyzed is the axial tension test. This test involved the use of the push rod method to apply an axial force onto the test sample. Using two strain gauges to read strain as opposed to the single strain gauge setup in burst testing, as well as the previously mentioned measurement techniques, the sample data was measured and processed. The average PLS for the tension samples was 58.17 MPa, with an average failure stress of 191.23 MPa. These samples had the highest failures stresses of the whole batch, by a margin of around ~30 MPa. Below are the measurements for the axial samples tested, as well as the PLS, failure stresses, and stress angles. After that are the results for Tensile stress and strain, with AE results as well.

Table 3.3, Axial/Tension Sample Measurements

Sample #	ID (mm)	OD (mm)	A (mm^2)	J (mm^4)
19-2-A	7.595	9.106	19.82	348.37
19-2-B	7.557	9.093	20.09	351.12
19-2-C	7.582	9.093	19.79	346.79

Table 3.4, Axial/Tension Sample Stresses and Angles

	Principal stress MPa		Principal direction (degree)	
Sample #	PLS	UTS	PLS	UTS
19-2-A	67.50	196.88	90°	90°
19-2-B	53.09	187.70	90°	90°
19-2-C	53.92	189.10	90°	90°

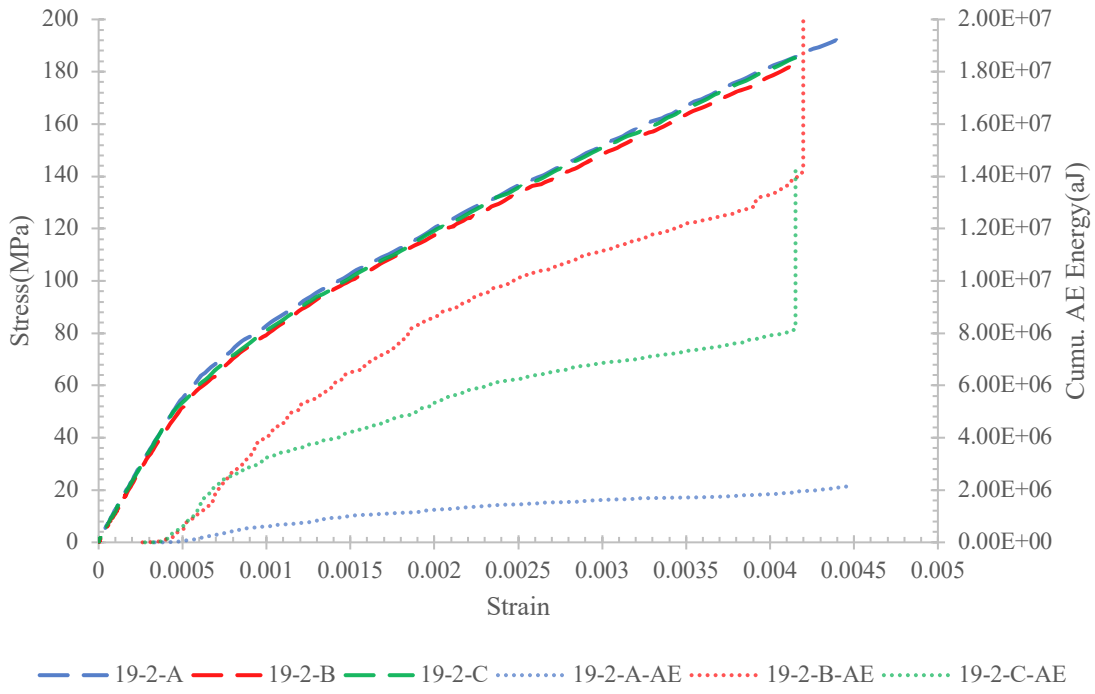

Figure 3.5, Tensile/axial stress-strain, AE results

The tensile test results were repeatable, with repeatable failure methods as well. These tests had the highest failure strength out of all of the tests in the batch, showing that the architecture of these braids were strongest in tension. The AE results had a similar behavior to the burst test samples, with general scattered returns based on the application of the bonding material to the samples. However, calculations to assist in finding the PLS were still possible due to the AE being relative to the highest events recorded, with weaker signals still producing the same pattern by comparison to tests of higher strength.

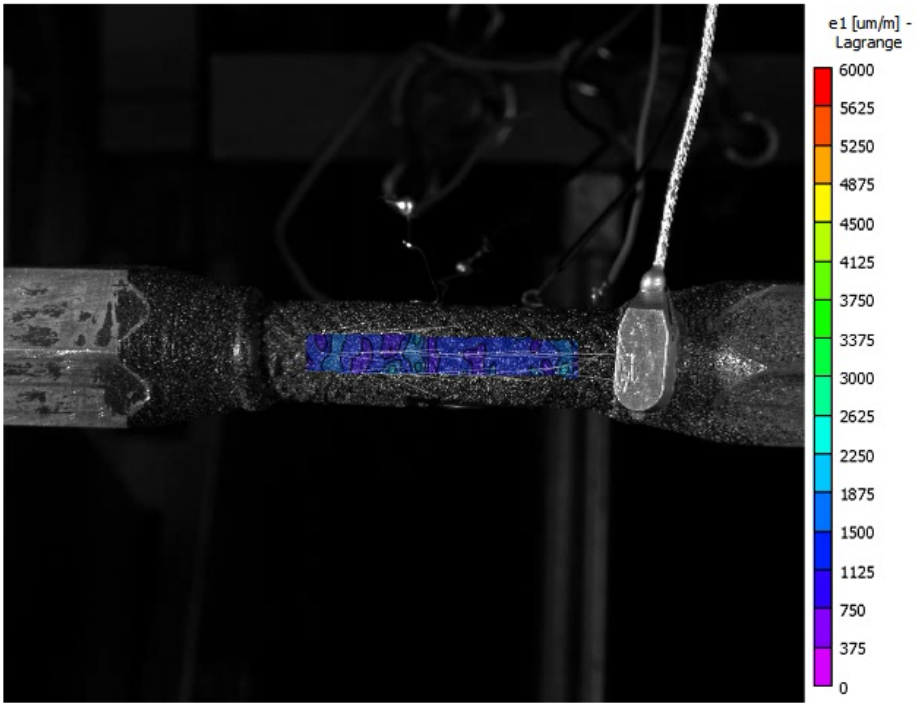

Figure 3.6, Tensile test DIC imaging vectors, principal strain(after test start)

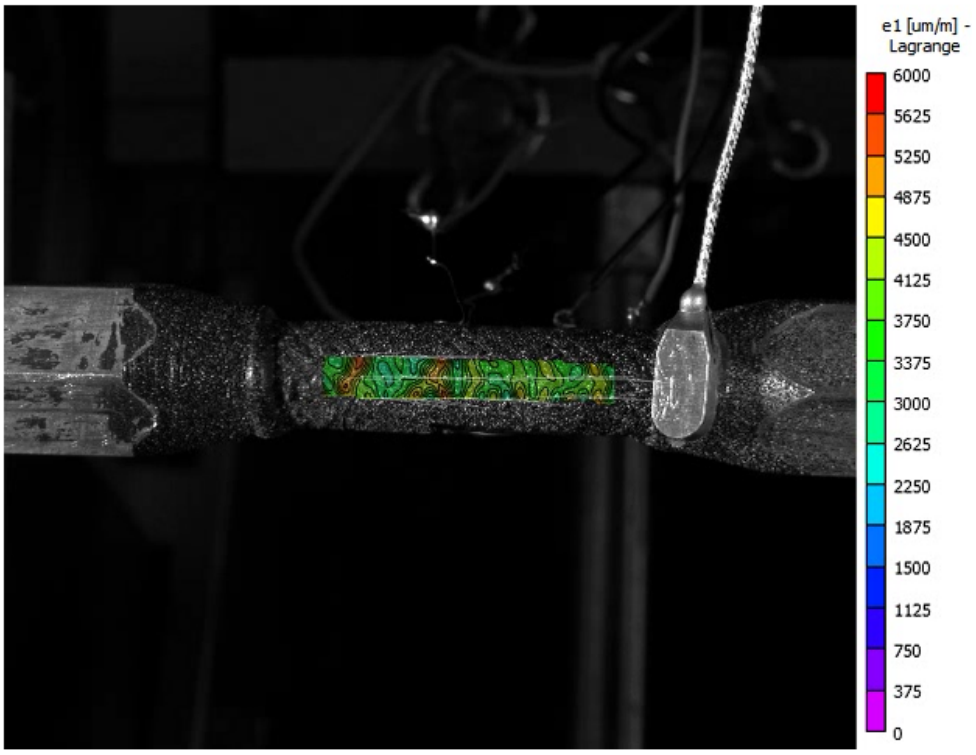

Figure 3.7, Tensile test DIC imaging vectors, principal strain(right before failure)

The next result pertaining to the tensile test were the DIC imaging results. This includes vectors potted on the DIC imaging to show the direction of the DIC strain on the sample. Two DIC image are shown for the tensile test samples, one showing behavior at the beginning of the test, and one right before failure. These can be seen in figure 3.6 and 3.7. This DIC imaging from this test shows a strain map that is characteristic of a tensile test. The angle of the load can be seen by the vector lines, which are 0° in the picture, but 90° relative to the failure envelope. This is consistent with the nature of this type of loading scenario.

Next, XCT imaging was applied to reveal the failure modes. The samples seemed to fail with a break that started along a perpendicular path to the direction of loading, and

leading to a less predictable pattern, with a similar behavior to the burst test with fragmenting along braid lines to a certain degree. The samples generally showed a pattern that displayed a weakness in the diagonal braids of the sample, at around 45° line compared to loading. This can be seen in figure 3.8:

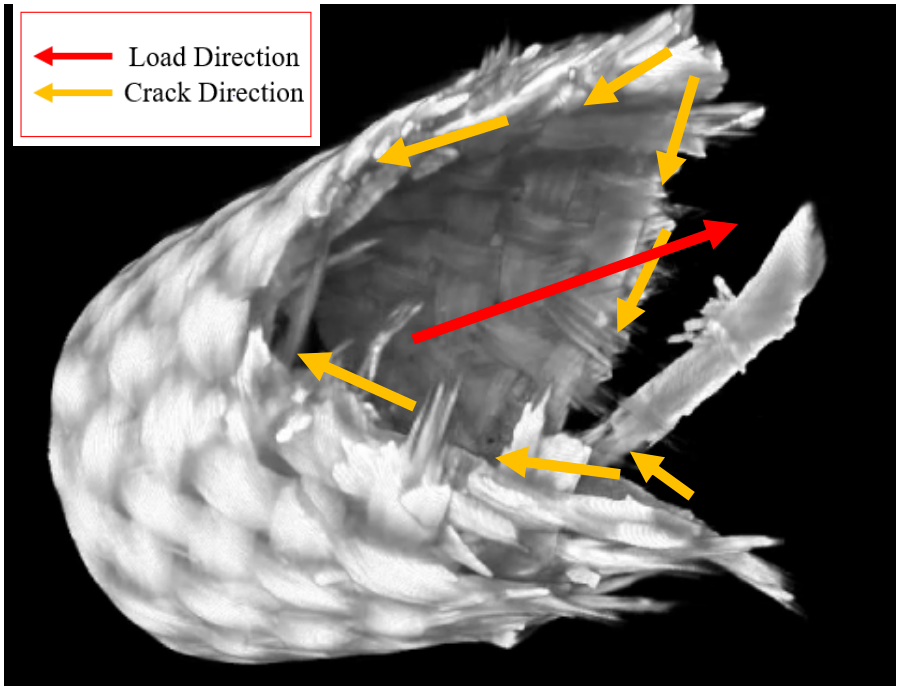

Figure 3.8, Tension test failure XCT scan

3.3 Torsion Loading Test

Next is the torsion tests. These samples were prepared according to the process for the torsion samples, and the test was set up and tested using the measurement procedure previously mentioned. The torsion samples ended up being the weakest failures stress among the 5 loading methods, with an average PLS of 19.07 MPa, and an average failure stress of 43.62 MPa. Below are the measurement values for the samples tested in torsion, as well as the stresses and stress/principal loading angles for the samples.

Table 3.5, Torsion sample measurements

Sample #	ID (mm)	OD (mm)	A (mm^2)	J (mm^4)
19-3-A	7.595	9.081	19.46	340.87
19-3-B	7.607	9.081	19.30	338.68
19-3-C	7.620	9.081	19.15	336.48
736-1-C	7.645	9.042	18.30	320.91
25-1-C	7.557	9.081	19.91	347.38

Table 3.6, Torsion sample stresses and angles

	Principal Stress MPa		Principal direction (degree)	
Sample #	PLS	UTS	PLS	UTS
19-3-A	19.48	43.58	45°	45°
19-3-B	15.32	43.20	45°	45°
19-3-C	20.10	46.29	45°	45°
736-1-C	18.32	43.27	45°	45°
25-1-C	22.14	41.79	45°	45°

As was stated previously, the AE data can vary from test to test, but still is able to be used to help find PLS data for samples. The torsion loading samples were the weakest samples of all the loading conditions for this triaxially braided sample type. However, it can also be said that they had the highest PLS when compared as a ratio of the UTS, and all of the torsion samples failed in graceful manners that did not cause much visible damage to the sample. These samples showed a very repeatable failure threshold and failure modes when tested, and after the initial reaction of weakness in the sample, the torsion test was highlighted and ran a second set in order to ensure the results were correct. There is a noticeable lag in the beginning of the data, which is attributed to noise and load readout

lag due to friction the load cell setup for torsional loading. This effect shows up in later combined loading data as well, albeit to a lesser degree as the effect of it is much lower in a combined loading state. The data found in this manner still shows accurate data for failure stress, and PLS data is still calculated in the same manner to the rest of the data sets.

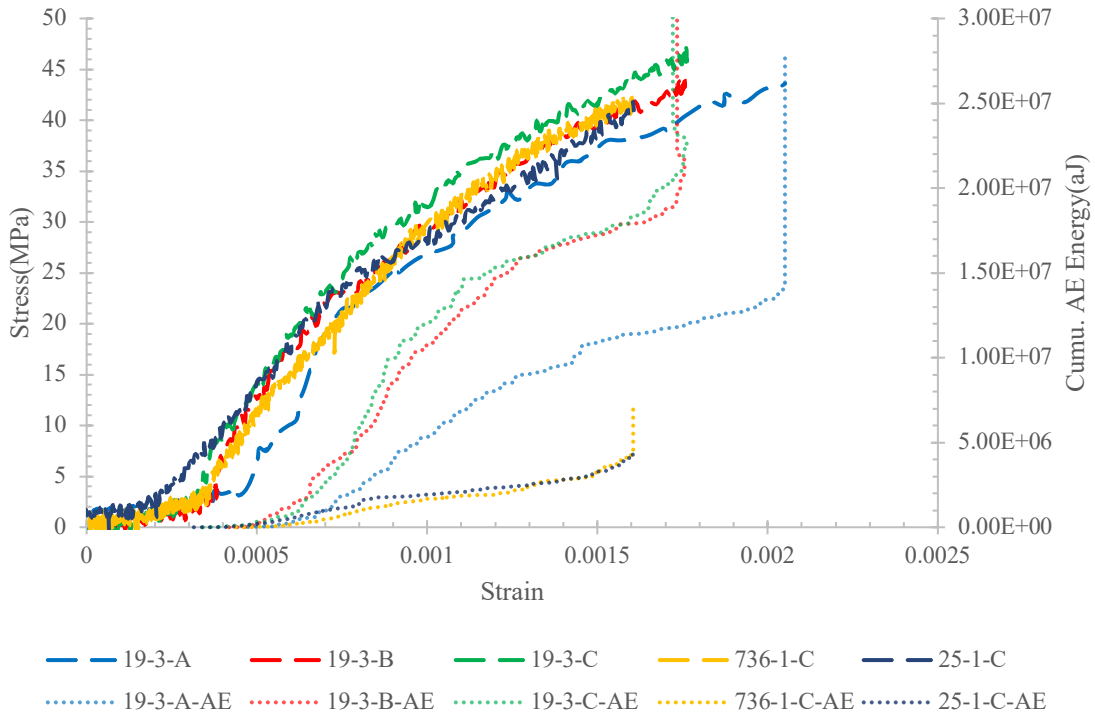

Figure 3.9, Torsion stress-strain, AE results

The next data to look at for this test type is the DIC imaging vectors to show location and direction of strain on the torsion samples. In figures 3.10 and 3.11, the torsion DIC can be seen. The DIC imaging vectors for this type of sample show a pure 45° angle of loading, as the pure torsion load on the sample exhibits a 45° principal stress angle when analyzed. The strain map shows the same perpendicular alignment to the areas of sample strain and strain pattern, showing the loading angle that in turn drives the sample to fail in such a manner.

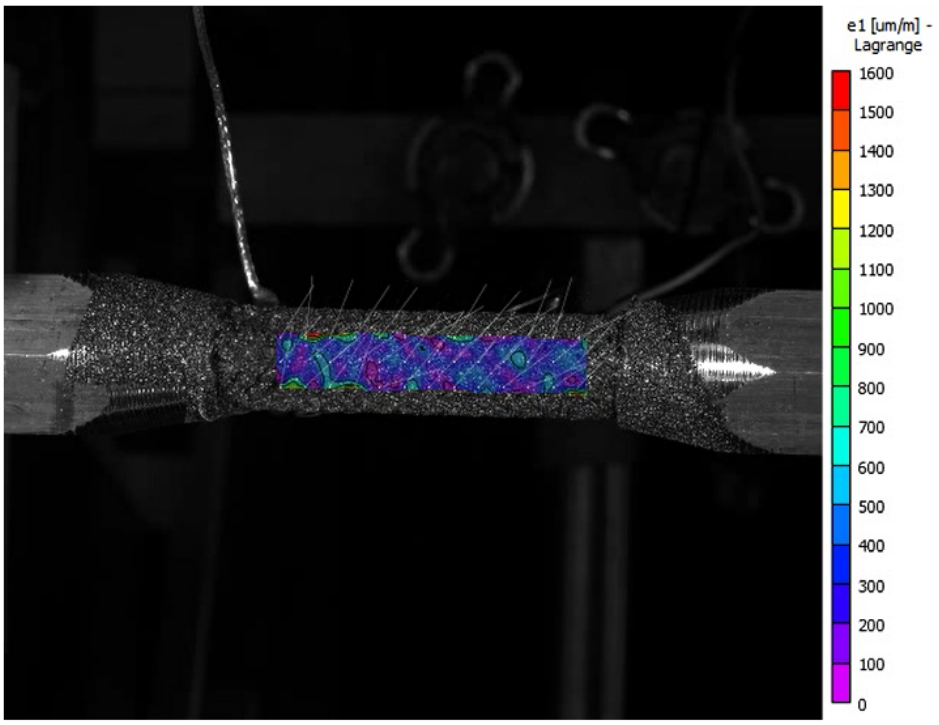

Figure 3.10, Torsion test DIC imaging vectors, principal strain(after test start)

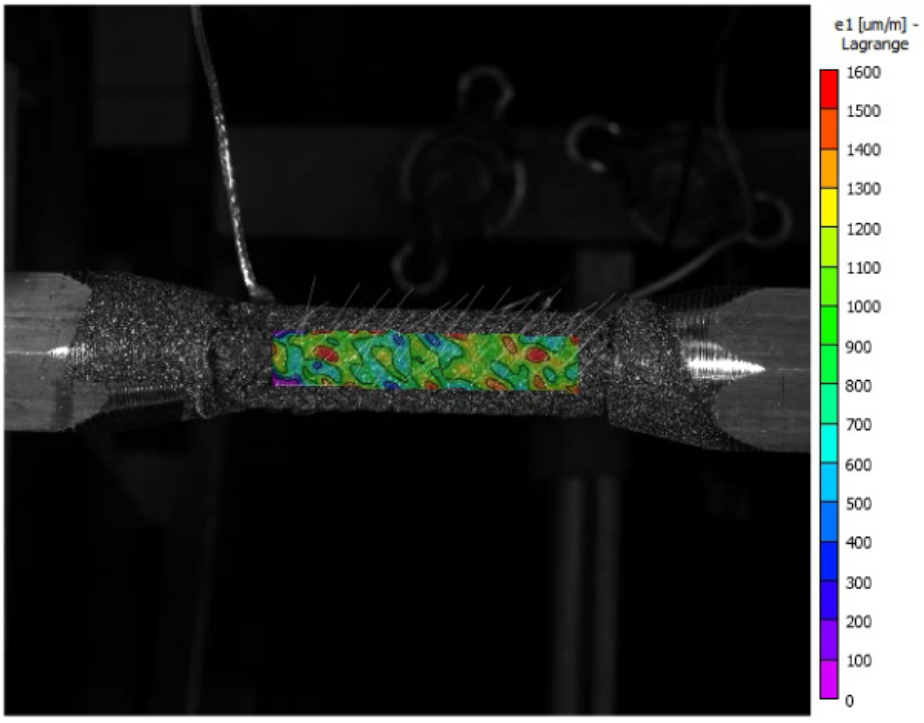

Figure 3.11, Torsion test DIC imaging vectors, principal strain(right before failure)

This 45° vector line was consistent across all torsion tests ran in this study. In all the cases of the torsion loading tests, the samples were still able to momentarily hold a stress level close to the recorded PLS after failure, which was different to all the other testing methods, as the final failure prohibited any residual stress on the samples after they broke.

In analyzing the XCT imaging of the torsion samples, the samples all showed a clean break line at a 45° angle, and had the least amount of damage, showing that the sample generally kept its full shape but lost its structural strength. Compared to the other tests, the XCT imaging was most needed to see a clear picture of failure for this loading condition compared to the other ones due to the lack of notable damage accumulation on the sample after failure.

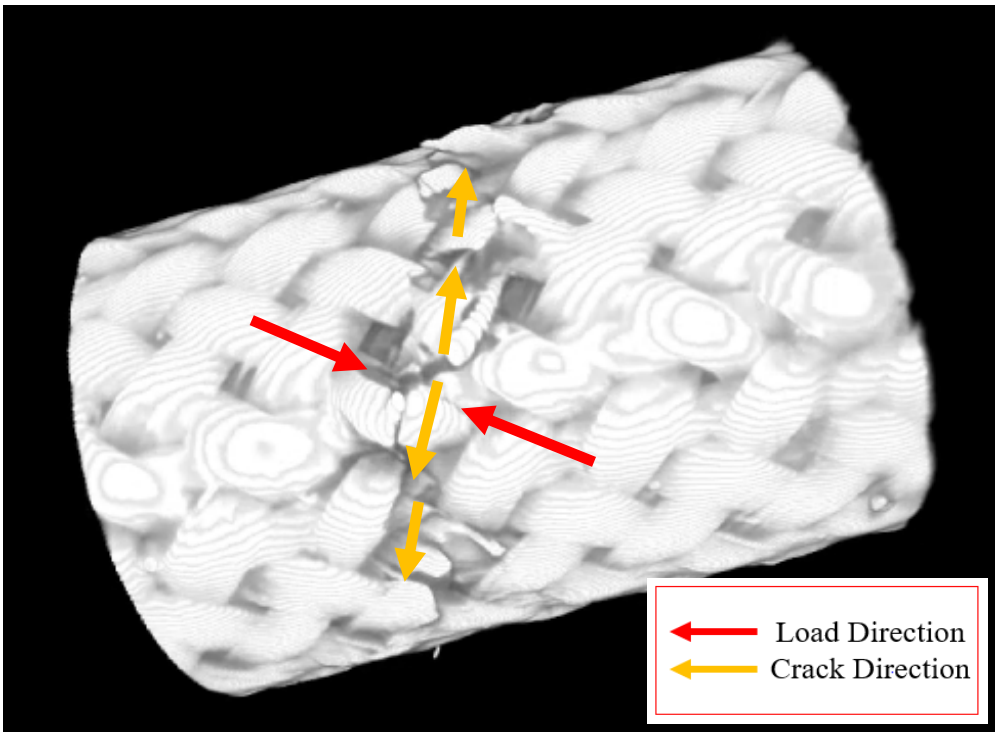

Figure 3.12, Torsion test failure XCT scan

The XCT scan of this can be seen in figure 3.12, showing the 45° line of break along the sample that was stated previously. The red line indicates the angle/direction of load on the sample, and can be seen as the compressive part of the torsion loading setup. In torsion, one 45° direction experiences tensile loading, and the other 45° angle(90° from the tensile 45°) experiences a compressive load. The compressive load is what caused these samples to locally buckle, compared to all the other samples, which was something to be noted. The sample followed the ongoing trend of previous tests in this batch to break along the 45° direction, although this was expected for a 45° principal stress loading angle.

3.4 Torsion-Burst Loading Test

The 4th test analyzed was the torsion-burst, or internal pressure torsion test. These samples were prepared according to the process for preparing the torsion-burst samples, and ran in the testing rig setup. These samples, when setup, were ran with an attempted 50/50 failure method in mind for the failure. Using the previously mentioned control program to control load, a ratio was selected at first to see if the pre-test calculations were correct. The load ratios were tweaked slightly at times based on reactions in the test, with a general goal to also keep the samples within a comparable cluster of data points. The samples were tested using the previously mentioned procedure and analyzed after testing concluded. After testing, it was found that the samples had an average PLS of 24.6 MPa, and an average failure stress of 114.53 MPa. These samples had a failure mode that seemed to be an even combination of the burst and torsion methods. In tables 3.7 and 3.8, the measurements for all samples in this test set can be found, as well as all stresses and loading angles.

Table 3.7, Torsion-burst sample measurements

Sample #	ID (mm)	OD (mm)	A (mm^2)	J (mm^4)
181-2-D	7.518	8.992	19.10	328.03
181-1-C	7.582	9.068	19.43	339.33
181-1-D	7.595	9.119	20.00	352.15
181-2-C	7.518	9.055	20.00	346.35

Table 3.8, Torsion-burst sample stresses and angles

	Principal stress MPa		Principal direction (degree)	
Sample #	PLS	UTS	PLS	UTS
181-2-D	22.50	117.14	18.79°	18.41°
181-1-C	29.93	105.43	8.57°	18.57°
181-1-D	21.61	124.41	19.95°	19.79°
181-2-C	24.38	111.14	21.34°	20.00°

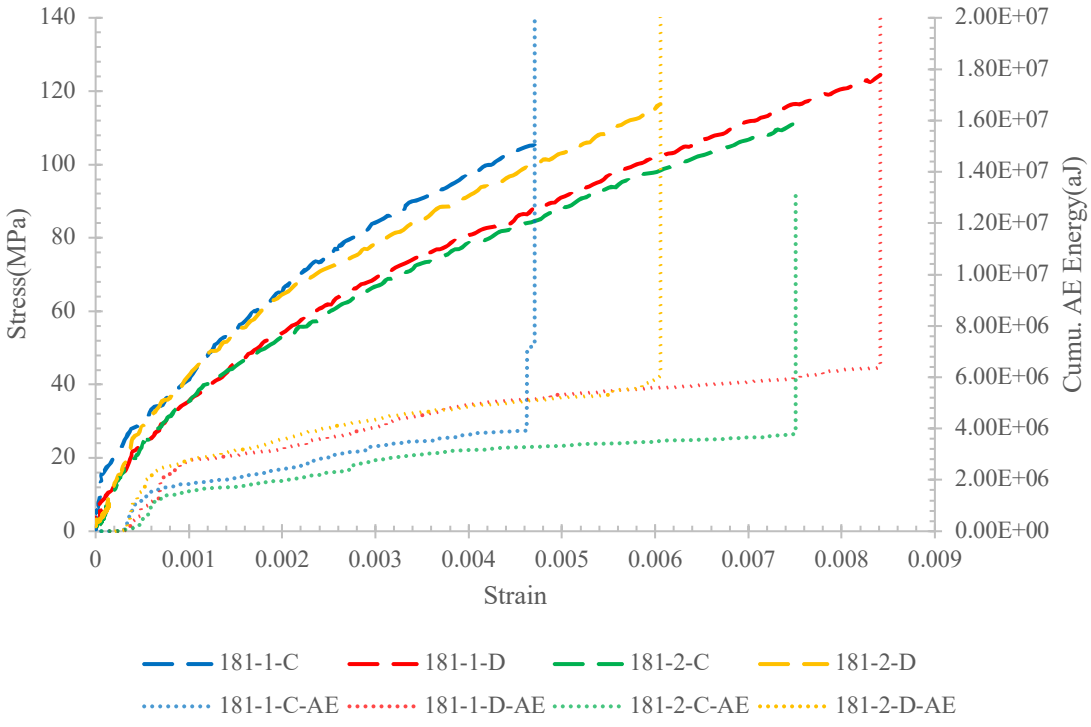

Figure 3.13, Torsion-burst stress-strain, AE results

In Figure 3.13 and table 3.8 are the Stress-Strain and AE results for the burst-torsion samples. In this set of samples ran in this manner, there is a noticeable outlier in sample 181-1-C. This is because of a failure in the loading program that was found and addressed, which allowed the other samples to be ran properly. This sample is included in the set for comparison, however it should be noted that the sample had a higher PLS compared to the others due to a imbalance in the early loading stage that made it behave more in an internal pressure stress state, as can be seen by the ~8° load angle seen in the table. However, the sample then stabilized and had a failure that was more in the range of the rest of the samples.

The next part of the torsion burst samples analyzed is the DIC vector imaging. This can be seen in figures 3.14 and 3.15

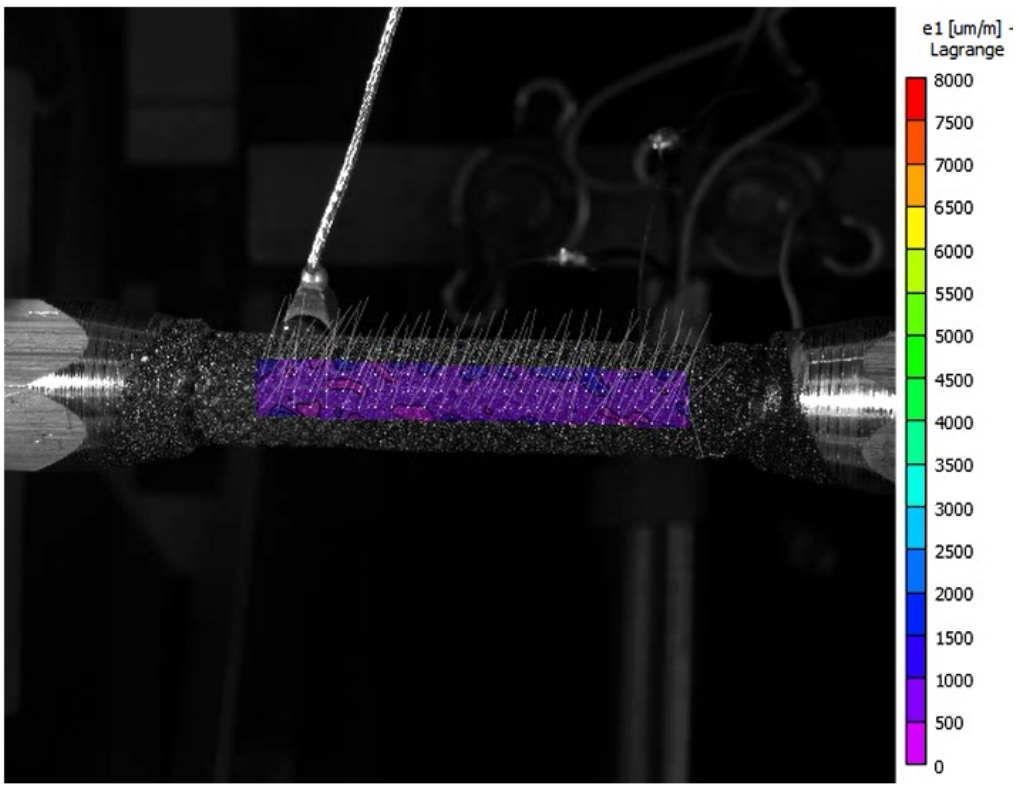

Figure 3.14, Torsion-burst DIC imaging vectors, principal strain(after test start)

In the torsion-burst DIC imaging, the combination of the loading methods can be characterized by the noticeable angle in the loading vectors. The angle is in between the previously shown torsion and burst methods, with those two angles being 90° and 45° on the DIC imaging respectively. The angle of the above test shows a clear split between the two different methods, as the angle in the DIC imaging is around 70° relative to the spine of the sample. This is representative of the ~19°-20° loading angles seen in the principal stress angle, representative of the loading direction for the torsion-burst samples.

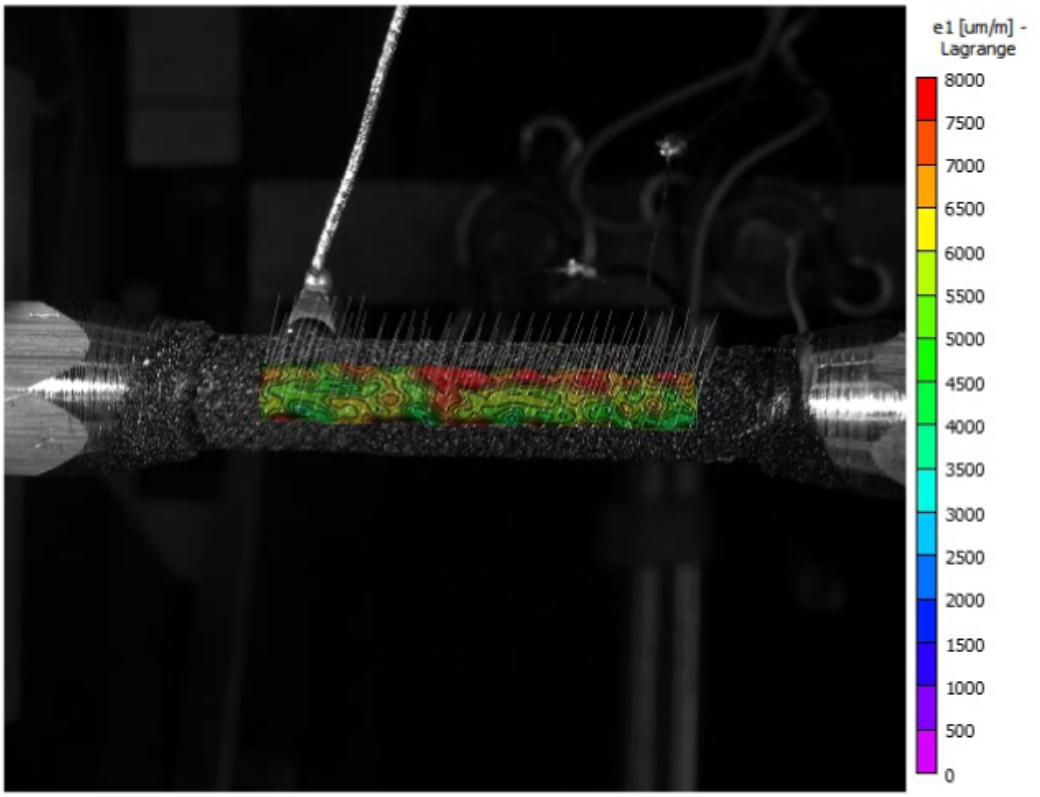

Figure 3.15, Torsion-burst DIC imaging vectors, principal strain(right before failure)

In analyzing the XCT images of the torsion-burst samples. these samples broke in a manner that was more indicative of the burst loading method, with small variances that

showed a torsion reaction as well. Generally, all the samples had a similar wide opening crack caused by the internal pressure failure, with various diagonal break lines as well, showing the reaction of the torsion loading. The cracks again showed a tendency to spread along diagonal weaker directions in the sample, started by the initial reaction for the internal pressure load opening up the sample. The red lines show the combined loading components, and the yellow lines show crack spread direction. This scan can be seen in Figure 3.16.

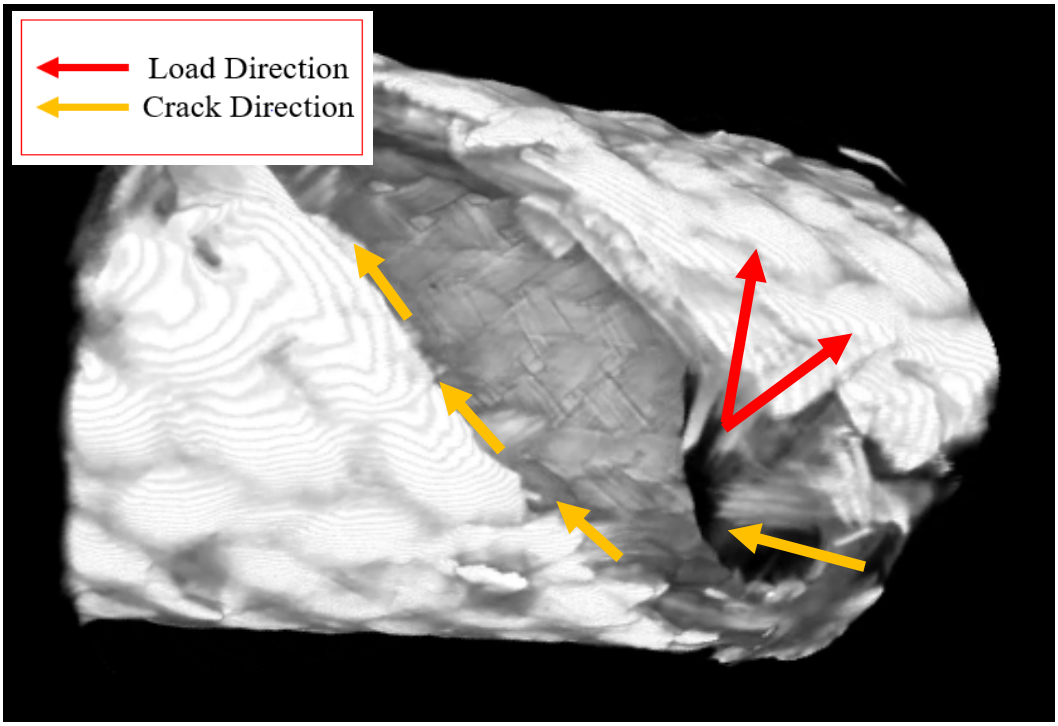

Figure 3.16, Torsion-burst failure XCT scan

3.5 Tension-Torsion Loading Test

Following a similar protocol to the torsion-burst combined loading test, the tension-torsion sample tests were carried out. These samples were ran and analyzed using the same

post processing steps used before in the previous tests. Using the load program designed for this test setup, the loading ratio between tension and torsion was calculated with a 50/50 break criteria between tension and torsion in mind. After running the tests, the actual angle of the principal stress was less than what had been calculated and planned for, with the samples failing more in tension than in torsion. However, these results were still promising to see the difference in how the torsion-burst samples reacted with torsional loading compared to this set, as differences can be seen regarding how more torsional loading can effect one of the more stronger loading conditions when applied together. With the samples ran and processed, the average PLS of the samples was 46.39 MPa, and the average failure stress was 158.238 MPa. Below are tables containing the sample measurements, and the samples stresses and principal load angles.

Table 3.9, Tension-torsion sample measurements

Sample #	**ID (mm)**	**OD (mm)**	**A (mm^2)**	**J (mm^4)**
736-1-A	7.645	9.068	18.67	328.32
736-1-B	7.620	9.093	19.33	340.22
25-1-A	7.582	9.042	19.06	331.92

Table 3.10, Tension-torsion sample stresses and angles

	Principal stress MPa		**Principal direction (degree)**	
Sample #	**PLS**	**UTS**	**PLS**	**UTS**
736-1-A	43.96	161.25	81.93°	81.72°
736-1-B	48.66	153.13	77.72°	79.32°
25-1-A	46.55	160.31	80.94°	80.33°

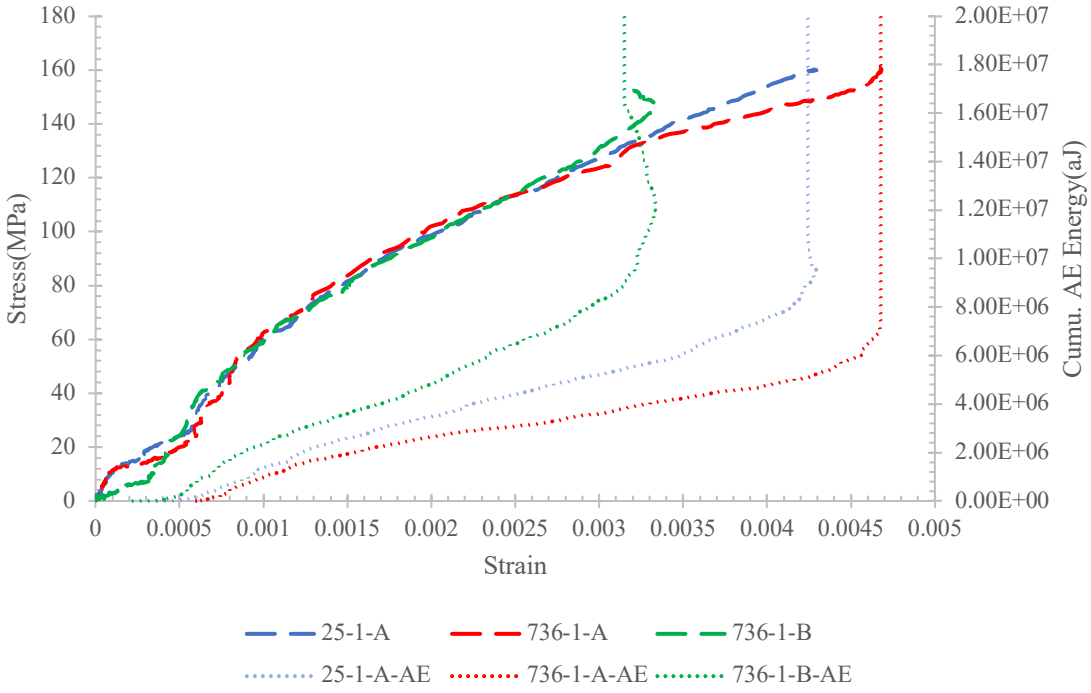

Figure 3.17, Tension-torsion stress-strain, AE results

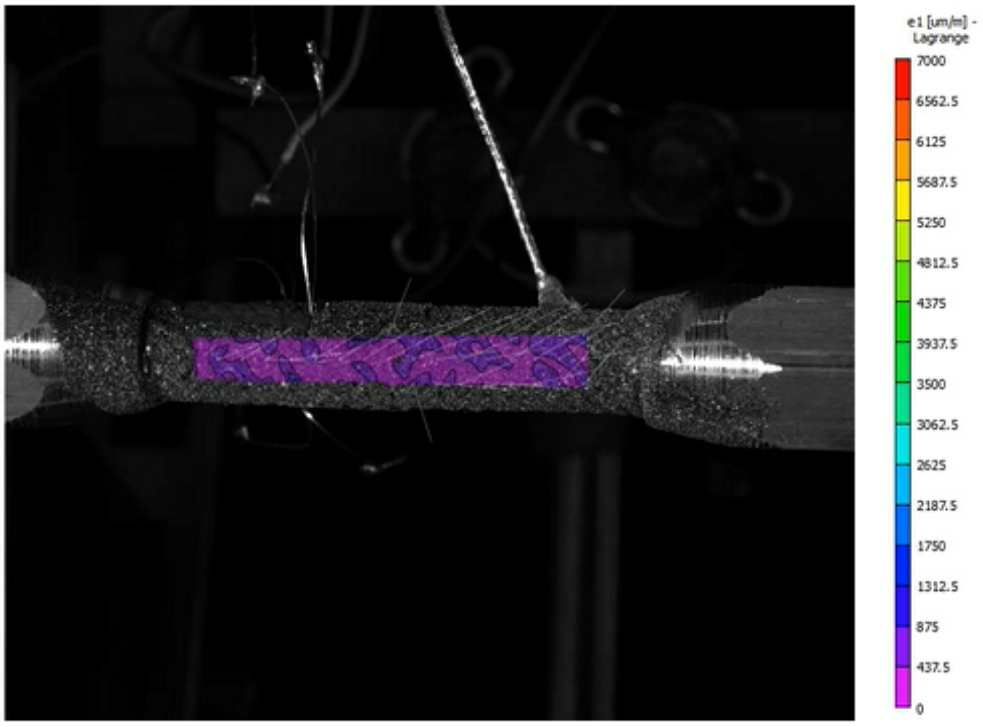

Figure 3.18, Tension-torsion DIC imaging vectors, principal strain(after test start)

The AE results for the tension-torsion test can be seen in figure 3.17, showing better consistency with the application of the AE sensor to the sample. The lag from the torsion method can be seen at the beginning of the sample, with the loading rounding out after a slight delay. PLS was calculated the same as the other samples mentioned before, using a combination of AE analysis and the loss of linearity in the material strength curve. These points can be seen in the previous tables seen before. The specific values for PLS and failure stresses can be seen detailed in table 3.10.

The next part of these samples that was analyzed were the DIC imaging vector plots. These show the angle induced from the applied stress on the sample, as well as the strains on the sample. The DIC imaging in the case of this testing setup showed repeatable results, with the angle shown on the DIC imaging to be consistent with a combined loading

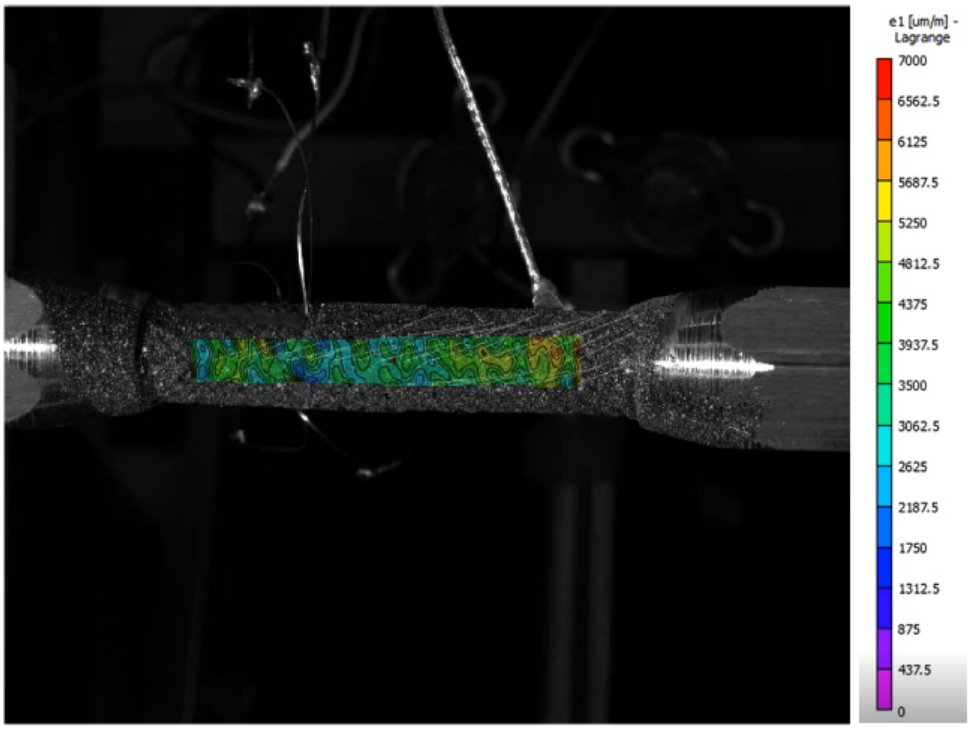

Figure 3.19, Tension-torsion DIC imaging vectors, principal strain(right before failure)

scenario of tension and torsion, in between the 0° for tension on DIC imaging and 45° for torsion. The image below shows an angle ~10° relative to the sample spine, consistent with the ~80° principal stress angle applied to the sample.

Addressing the XCT imaging results, these samples showed a failure mode that was mostly driven by the tensile loading, which is consistent with the amount of tensile stress applied in the testing. The samples had a reaction of failing in a tensile manner as seen previously in this study, with a slight interaction of the diagonal load failure that can be seen in the torsion loading methods. The XCT scan showed a similar trend to the rest of the loading conditions, with a mode of failure showing the weakness in the torsion direction and diagonal structure of the sample. This can be seen on figure 3.15, where the yellow arrow shows the crack direction and the red line show the combined loading applied.

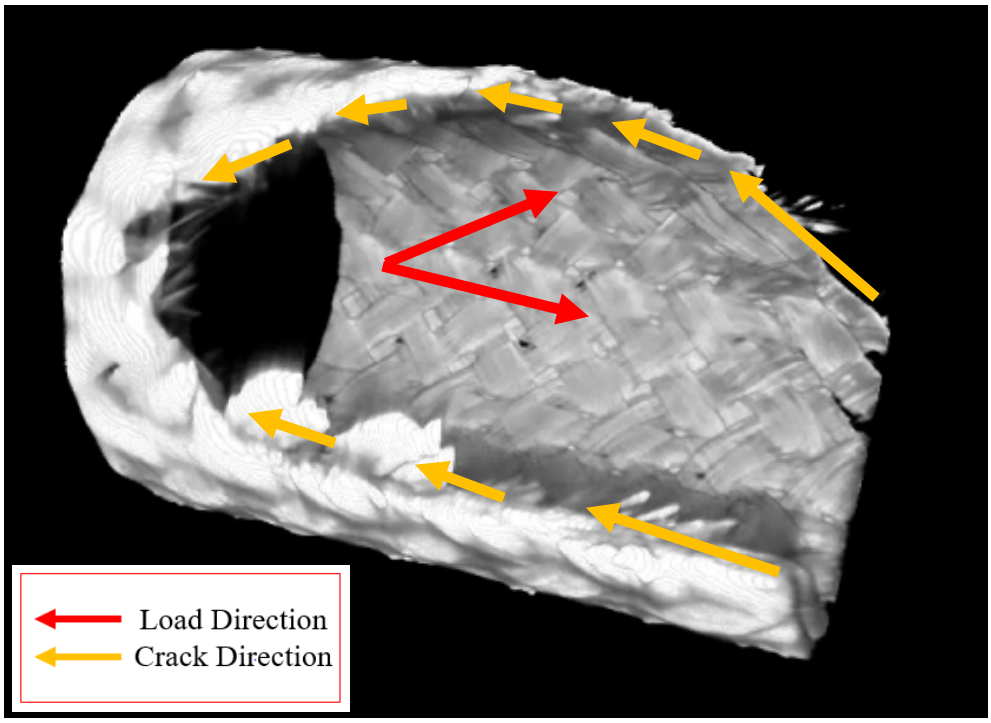

Figure 3.20, Tension-torsion failure XCT scan

3.6 Failure Envelope/Profile

The final developed failure profile for the samples tested was formed after all the samples were analyzed. Using post processing tools, a graph was created to show the reaction of the material to different types of loading in the study. This can be seen below, showing both the sample PLS points as well as the sample UTS points. The general failure envelope shape is that of a butterfly wing, showing two ellipsoid shapes starting at both axes that comes together at the failure points for the torsion-only failure:

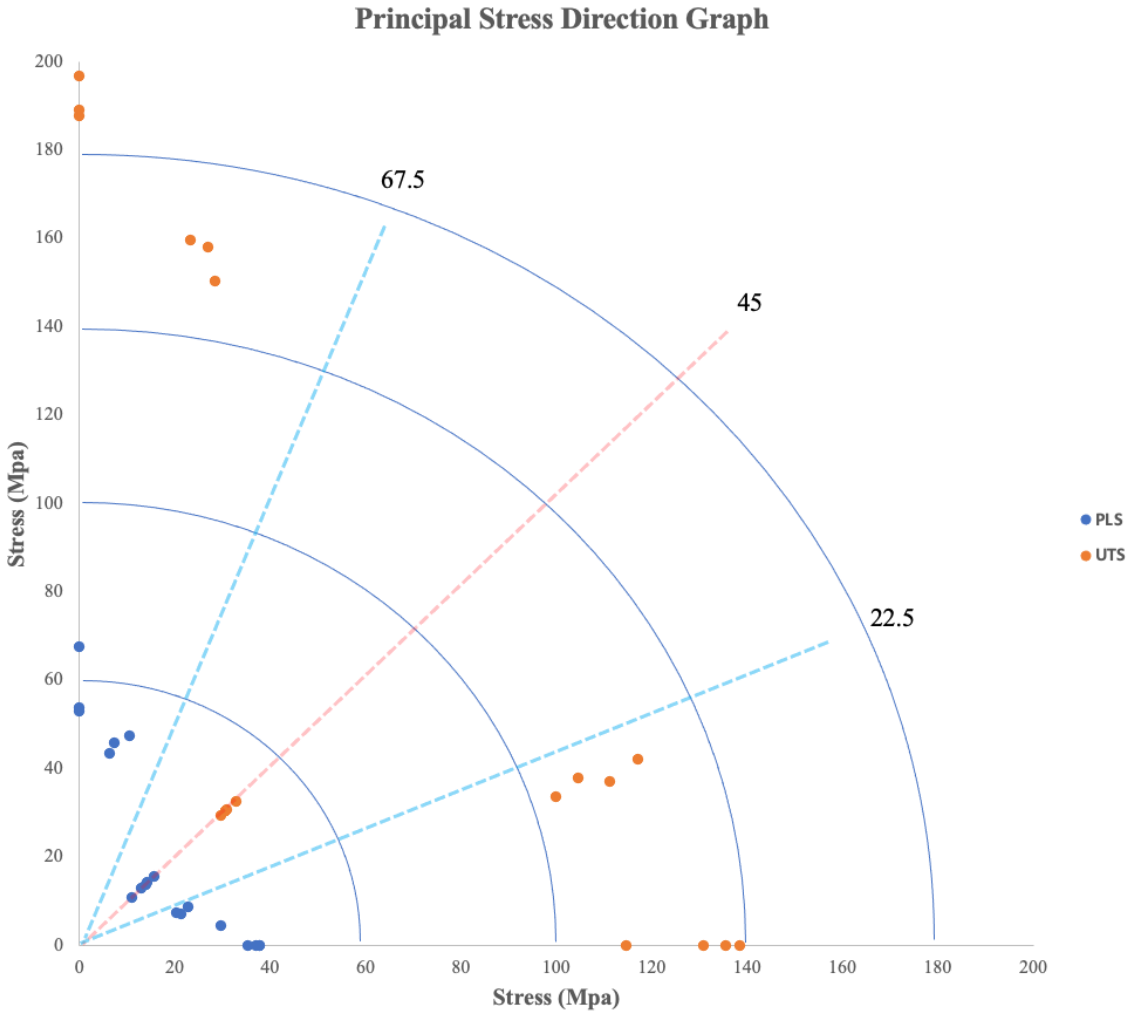

Figure 3.21, Empirical failure profile of triaxial SiC cladding

The failure profile that can be seen above is in terms of the principal stress direction on the samples, which was a result of the different loading conditions on the samples. At the 45° direction of principal stress on the sample, the samples were the weakest, showing weakness when in pure torsion, which results in a 45° principal stress angle on the sample. When this loading condition was then applied to the tensile or internal pressure methods, to form the combined loading methods shown in this study, it could be seen that it caused a notable strength loss as a result, compared to the uniaxial results for both tension and internal pressure. The samples were strongest in tension, which is figured to be the case due to the architecture of braids along the sample material, which has a braid angle that is more along the axial direction as can been seen in sample images and XCT scans shown previously.

CHAPTER 4. CONCLUSION

In this study, various uniaxial and multiaxial mechanical testing methods were developed and applied on a SiC_f/SiC_m triaxially braided cladding. These testing methods were validated using aluminum dummy samples. These measure the mechanical properties of aluminum samples matched well to the well known values. Using these methods, the cladding samples were tested to generate a failure envelope for this batch of samples. After creating a failure profile to address the overall strength profile, trends of strength behavior could be seen when combining two test methods together in multiaxial testing. The combined loading methods were shown to be effective in steering the principal stress direction, from a full range of 0°-90°relative to axial direction of the sample. In addition to stress and strain measurement from the combined loading test, for each sample, acoustic emission monitoring was applied to help determine the proportion limit stress (PLS), digital image correlation was applied to visualize full-field strain and determine the principal stress direction. After, X-ray tomography was applied to characterize the damage and failure modes.. By using all of these methods, the anisotropic nature of the sample strength could be analyzed. The PLS values for when samples started to degrade past the point of elastic behavior on the sample could be found by the onset of the first loud AE event. The UTS values for final failure were determined by the have final failure values for stress and strain. Using these PLS and UTS values, the failure envelope was then formed to show the entire profile of samples studied. It was found after testing that the triaxially-braided SiC_f/SiC_m cladding material was strongest in tension, and was weakest in torsion.

REFERENCES

[1] Kirill Shapovalov, George M. Jacobsen, Luis Alva, Nathaniel Truesdale, Christian P. Deck, Xinyu Huang, “Strength of SiCf-SiCm composite tube under uniaxial and multiaxial loading”, Journal of Nuclear Materials, Volume 500, 2018, Pages 280-294, ISSN 0022-3115.

[2] Fabien Bernachy-Barbe, Lionel Gélébart, Michel Bornert, Jérôme Crépin, Cédric Sauder, “Anisotropic damage behavior of SiC/SiC composite tubes: Multiaxial testing and damage characterization”, Composites Part A: Applied Science and Manufacturing, Volume 76, 2015, Pages 281-288, ISSN 1359-835X.

[3] Rhodes, Christopher, “The Fukushima Daiichi Nuclear Accident”, Science progress, (2014), 97. 72-86.

[4] Masaki Kurata, “Research and Development Methodology for Practical Use of Accident Tolerant Fuel in Light Water Reactors”, Nuclear Engineering and Technology, Volume 48, Issue 1, 2016, Pages 26-32, ISSN 1738-5733.

[5] Lars Hallstadius, Steven Johnson, Ed Lahoda, “Cladding for high performance fuel, Progress in Nuclear Energy”, Volume 57, 2012, Pages 71-76, ISSN 0149-1970.

[6] C.P. Deck, H.E. Khalifa, B. Sammuli, T. Hilsabeck, C.A. Back, “Fabrication of SiC–SiC composites for fuel cladding in advanced reactor designs”, Progress in Nuclear Energy, Volume 57, 2012, Pages 38-45, ISSN 0149-1970.

[7] Yangbin Deng, Bowen Qiu, Bo Pang, Xing Gong, Yingwei Wu, Guanghui Su, Xi Huang, Yongchun Li, Yuan Yin, “Research on performance enhancement of nuclear fuel with SiC cladding by using high thermal conductivity fuels”, Progress in Nuclear Energy, Volume 124, 2020, 103330, ISSN 0149-1970.

[8] C.P. Deck, G.M. Jacobsen, J. Sheeder, O. Gutierrez, J. Zhang, J. Stone, H.E. Khalifa, C.A. Back, “Characterization of SiC–SiC composites for accident tolerant fuel cladding”, Journal of Nuclear Materials, Volume 466, 2015, Pages 667-681, ISSN 0022-3115.

[9] C. Fellah, J. Braun, C. Sauder, F. Sirotti, M.-H. Berger, “Influence of the carbon interface on the mechanical behavior of SiC/SiC composites”, Composites Part A: Applied Science and Manufacturing, Volume 133, 2020, 105867, ISSN 1359-835X.

[10] S.L. Ogin, P. Potluri, “1 - Textile-reinforced composite materials”, Editor(s): A. Richard Horrocks, Subhash C. Anand, Handbook of Technical Textiles (Second Edition), Woodhead Publishing, 2016, Pages 1-26, ISBN 9781782424659.

[11] Omega, “Practical Strain Gage Measurements” 1999. https://www.omega.co.uk/techref/pdf/StrainGage_Measurement.pdf

[12] Rescalvo, Francisco & Valverde-Palacios, I. & Suarez Vargas, Elisabet & Roldan, Andres & Gallego, Antolino. (2018). Monitoring of Carbon Fiber-Reinforced Old Timber Beams via Strain and Multiresonant Acoustic Emission Sensors. Sensors. 18. 1224. 10.3390/s18041224.

[13] Gregory N. Morscher, “Modal acoustic emission of damage accumulation in a woven SiC/SiC composite”, Composites Science and Technology, Volume 59, Issue 5, 1999, Pages 687-697, ISSN 0266-3538.

[14] E. Maillet, N. Godin, M. R’Mili, P. Reynaud, G. Fantozzi, J. Lamon, “Damage monitoring and identification in SiC/SiC minicomposites using combined acousto-ultrasonics and acoustic emission”, Composites Part A: Applied Science and Manufacturing, Volume 57, 2014, Pages 8-15, ISSN 1359-835X.

[15] Shanhua Liu, Litong Zhang, Xiaowei Yin, Yongsheng Liu, Laifei Cheng, “Proportional Limit Stress and Residual Thermal Stress of 3D SiC/SiC Composite”, Journal of Materials Science & Technology, Volume 30, Issue 10, 2014, Pages 959-964, ISSN 1005-0302.

[16] Takashi Nozawa, Kazumi Ozawa, Hiroyasu Tanigawa, “Re-defining failure envelopes for silicon carbide composites based on damage process analysis by acoustic emission”, Fusion Engineering and Design, Volume 88, Issues 9–10, 2013, Pages 2543-2546, ISSN 0920-3796.

[17] Brendan P. Croom, Peng Xu, Edward J. Lahoda, Christian P. Deck, Xiaodong Li, “Quantifying the three-dimensional damage and stress redistribution mechanisms of braided SiC/SiC composites by in situ volumetric digital image correlation”, Scripta Materialia, Volume 130, 2017, Pages 238-241, ISSN 1359-6462.

[18] Frederick M. Heim, John T. Daspit, Oliver B. Holzmond, Brendan P. Croom, Xiaodong Li, “Analysis of tow architecture variability in biaxially braided composite tubes”, Composites Part B: Engineering, Volume 190, 2020, 107938, ISSN 1359-8368.

[19] Travis Whitlow, Eric Jones, Craig Przybyla, “In-situ damage monitoring of a SiC/SiC ceramic matrix composite using acoustic emission and digital image correlation”, Composite Structures, Volume 158, 2016, Pages 245-251, ISSN 0263-8223.

[20] Yang Chen, Yuan Shi, Camille Chateau, James Marrow, “In situ X-ray tomography characterisation of 3D deformation of C/C-SiC composites loaded under tension”, Composites Part A: Applied Science and Manufacturing, Volume 145, 2021, 106390, ISSN 1359-835X.

[21] Yuan Chai, Ying Wang, Zeshan Yousaf, Nghia T. Vo, Tristan Lowe, Prasad Potluri, Philip J. Withers, “Damage evolution in braided composite tubes under torsion studied by in-situ X-ray computed tomography”, Composites Science and Technology, Volume 188, 2020, 107976, ISSN 0266-3538.

[22] Valentina Angelici Avincola, Pierre Guenoun, Koroush Shirvan, “Mechanical performance of SiC three-layer cladding in PWRs”, Nuclear Engineering and Design, Volume 310, 2016, Pages 280-294, ISSN 0029-5493.

[23] J.G. Stone, R. Schleicher, C.P. Deck, G.M. Jacobsen, H.E. Khalifa, C.A. Back, “Stress analysis and probabilistic assessment of multi-layer SiC-based accident tolerant nuclear fuel cladding”, Journal of Nuclear Materials, Volume 466, 2015, Pages 682-697, ISSN 0022-3115.

[24] Xinran Xiao, Hamid G. Kia, Xiao-Jing Gong, “Strength prediction of a triaxially braided composite”, Composites Part A: Applied Science and Manufacturing, Volume 42, Issue 8, 2011, Pages 1000-1006, ISSN 1359-835X.

[25] G.M. Jacobsen, J.D. Stone, H.E. Khalifa, C.P. Deck, C.A. Back, “Investigation of the C-ring test for measuring hoop tensile strength of nuclear grade ceramic composites”, Journal of Nuclear Materials, Volume 452, Issues 1–3, 2014, Pages 125-132, ISSN 0022-3115.

[26] Gregory N. Morscher, Mrityunjay Singh, J. Douglas Kiser, Marc Freedman, Ram Bhatt, “Modeling stress-dependent matrix cracking and stress–strain behavior in 2D woven SiC fiber reinforced CVI SiC composites”, Composites Science and Technology, Volume 67, Issue 6, 2007, Pages 1009-1017, ISSN 0266-3538.

[27] ASTM C1773-21, Standard Test Method for Monotonic Axial Tensile Behavior of Continuous Fiber-Reinforced Advanced Ceramic Tubular Test Specimens at Ambient Temperature, ASTM International, West Conshohocken, PA, 2021, www.astm.org.

[28] P. Potluri, A. Manan, M. Francke, R.J. Day, “Flexural and torsional behaviour of biaxial and triaxial braided composite structures”, Composite Structures, Volume 75, Issues 1–4, 2006, Pages 377-386, ISSN 0263-8223.

[29] Lance L. Snead, Takashi Nozawa, Yutai Katoh, Thak-Sang Byun, Sosuke Kondo, David A. Petti, “Handbook of SiC properties for fuel performance modeling”, Journal of Nuclear Materials, Volume 371, Issues 1–3, 2007, Pages 329-377, ISSN 0022-3115.

[30] Akira Kohyama, Joon-Soo Park, Hun-Chea Jung, “Advanced SiC fibers and SiC/SiC composites toward industrialization”, Journal of Nuclear Materials, Volume 417, Issues 1–3, 2011, Pages 340-343, ISSN 0022-3115.